nature communications

Article

https://doi.org/10.1038/s41467-025-66164-2

Body-wide synchronization of insulin-signaling dependent DAF-16/FOXO nuclear translocation pulses correlated with *C. elegans* growth

Received: 16 January 2024

Accepted: 29 October 2025

Burak Demirbas[1,5], Olga Filina[1,5], Timo Louisse[1], Ananya Natarajan[1], Yvonne Goos[1], María Antonia Sánchez-Romero[2], María Olmedo[3] & Jeroen S. van Zon[1,4]

Insulin signaling is the core pathway regulating body growth, but the dynamics of insulin signaling across an organism has not been studied experimentally. By imaging *C. elegans* larvae in microchambers, we follow the key insulin signaling step, DAF-16/FOXO nuclear translocation, at cellular level throughout the body. We show that under constant stress, translocation occurs in stochastic pulses, but with each translocation pulse occurring near-simultaneously in all cells. Pulsatile DAF-16/FOXO translocation is correlated with growth, as periods of long or frequent pulses coincide with bouts of growth arrest, and short, infrequent pulses with body growth, while the animal's ability to arrest growth is lost in *daf-16/FOXO* mutants. Organism-wide coordination of DAF-16/FOXO translocation pulses might thus be important to ensure uniformity of body growth, with potential implications for understanding tissue- and body-wide coordination of insulin-dependent processes also in humans.

Insulin/insulin-like growth factor signaling (IIS) is a key pathway regulating body growth under normal[1–4] and stressed conditions[5–7]. Growth control occurs through FOXO transcription factors[8] that, upon loss of IIS activity, translocate to the nucleus, where they control downstream gene expression[1,9–12]. Growth uniformity is generally assumed to follow from body-wide spreading of insulins through passive mechanisms, such as release into the circulation and diffusion[13,14]. Tissue- or body-wide coordination is crucial also for other insulin-dependent processes, such as control of glucose metabolism by blood insulin[15], with impact on diabetes, obesity and longevity[16–19]. However, the dynamics of insulin signaling across an entire animal has not been studied experimentally.

To investigate organism-wide dynamics of DAF-16/FOXO, the sole *C. elegans* FOXO transcription factor (TF), we studied the *C. elegans* L1 arrest, a developmental arrest larvae enter when they encounter stress, including starvation, osmotic shock and heat, directly after hatching, and that is under control of IIS[7,20–24] (Fig. 1A). Under unstressed conditions, high insulin-like peptide (ILP) levels activate the insulin receptor DAF-2, causing phosphorylation and cytoplasmic localization of DAF-16/FOXO[25–27]. Upon stress, low ILP levels result in DAF-2 inactivation, DAF-16/FOXO dephosphorylation and its subsequent translocation into the nucleus, where it induces stress response genes[28–30] and regulators of cell proliferation[20], ultimately leading to developmental arrest. A puzzling result emerging from previous studies is that even under constant high stress, a substantial fraction (20–60%) of animals showed no or little nuclear DAF-16/FOXO[24,31,32], hinting at a so far unresolved variability in DAF-16/FOXO response between individual larvae.

---

[1]AMOLF, Amsterdam, the Netherlands. [2]Departamento de Microbiología y Parasitología, Universidad de Sevilla, Seville, Spain. [3]Departamento de Genética, Universidad de Sevilla, Seville, Spain. [4]Institute of Biology Leiden, Leiden University, Leiden, The Netherlands. [5]These authors contributed equally: Burak Demirbas, Olga Filina. e-mail: mariaolmedo@us.es; j.v.zon@amolf.nl

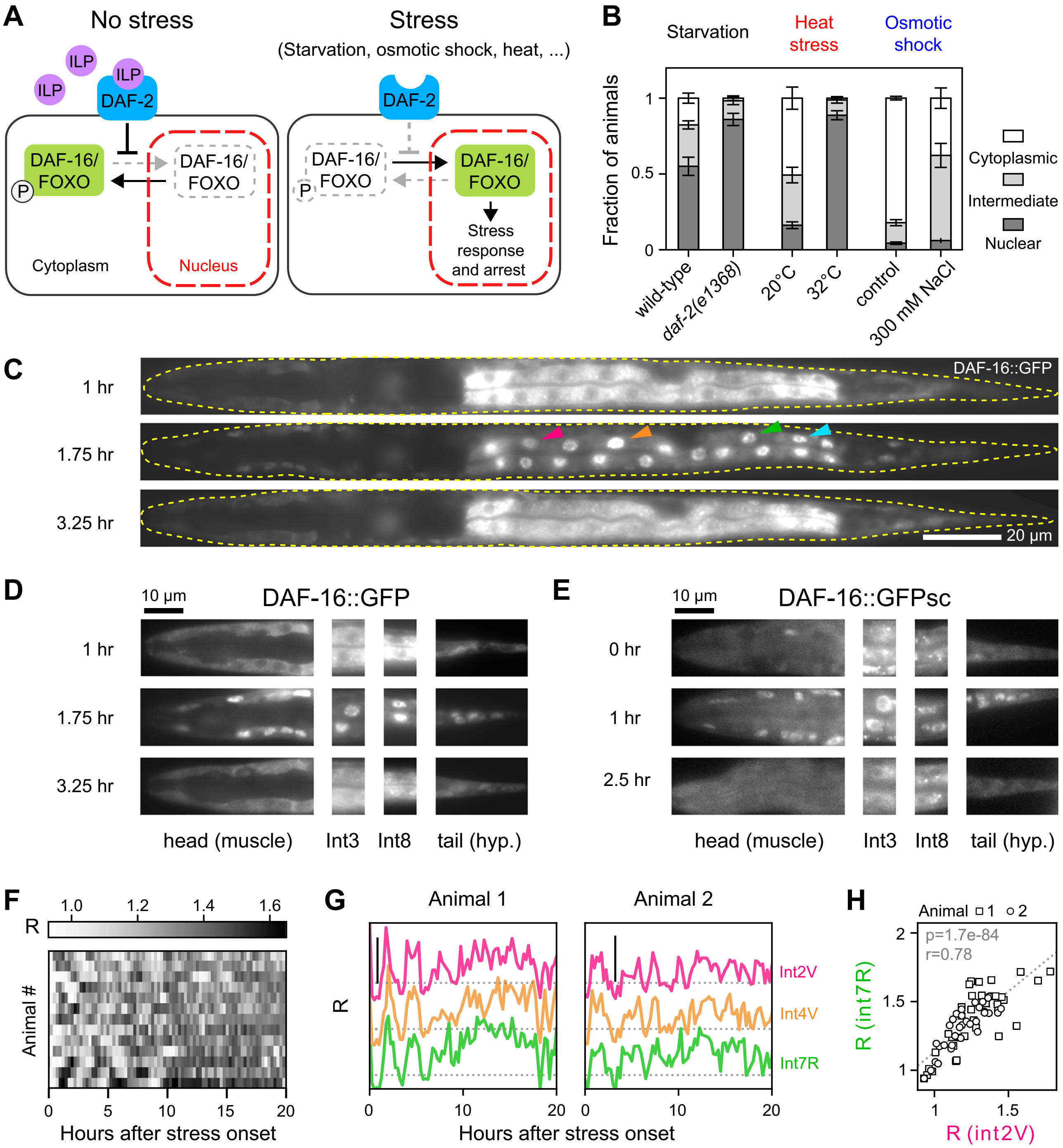

Fig. 1 | Stochastic, synchronized DAF-16/FOXO nuclear translocation pulses. **A** Schematic representation of the Insulin/insulin-like growth factor-1 signaling (IIS) pathway. **B** Fraction of L1 larvae with nuclear DAF-16::GFP localization for wild-type and *daf-2(e1368)* animals under starvation, and wild-type animals exposed to heat or osmotic shock. Fractions are calculated over $n = 367$ (starvation, wild-type), $n = 426$ (starvation, *daf-2*), $n = 194$ (heat stress, 20 °C), $n = 195$ (heat stress, 32 °C), $n = 254$ (osmotic shock, control) and $n = 199$ (osmotic shock, 300 mM NaCl) animals. Data are for 4 (starvation) or 3 replicates (heat stress, osmotic shock). Error bars are the standard error of the mean (S.E.M.) over replicates. **C** Straightened fluorescence images of a starved L1 animal, carrying a DAF-16::GFP integrated transgene, showing alternating nuclear and cytoplasmic DAF-16 localization. Hours indicate time after hatching in microchambers without food. Dashed yellow line indicates animal's outline. Scale bar: 20 μm. Arrowheads indicate intestinal cells Int2D/V (magenta), Int4D/V (orange), Int7L/R (green), and Int8L/R (cyan), used for single-cell quantification. **D**, **E** DAF-16::GFP nuclear translocation dynamics in head muscle cells, intestinal cells, or tail hypodermal cells upon constant starvation stress. Both for DAF-16::GFP (**D**) and a single-copy, endogenously-tagged DAF-16::GFPsc strain (**E**), translocation occurred in pulses that were synchronized between the different tissues. Scale bar: 10 μm. Images in **C**–**E** were computationally straightened for clarity. **F** Heatmaps of DAF-16::GFP nuclear localization *R*, calculated as the ratio of DAF-16::GFP intensity in the nucleus and cytoplasm, over time. Rows represent individual, starved animals. Color intensity corresponds to *R*, as averaged over all intestinal cells. **G** DAF-16::GFP nuclear localization *R* measured for different intestinal cells, for two starved individuals. Despite variability between individuals, *R* is synchronized between cells. Tracks are shifted along the y-axis for clarity. For each cell, dashed lines is $R = 1.03$, corresponding to 105% of the average *R* in non-stressed animals. Vertical black line corresponds to amplitude of 0.5. **H** Correlation of *R* for tracks for int2V and int7R in **G**, with Pearson correlation coefficient *r* and *p*-value (two-sided Wald test) indicated.

Here, we show that the key insulin signaling step, DAF-16/FOXO nuclear translocation, occurs throughout the *C. elegans* body in stochastic, yet highly synchronized pulses, that correlate with the animal's growth state. By imaging *C. elegans* larvae locked in microchambers, we follow DAF-16/FOXO nuclear translocation over time, at the cellular level throughout the body. Under constant stress, translocation is pulsatile, with dynamics depending on stress type and magnitude, while each translocation pulse occurs near-simultaneously in all cells. These synchronized DAF-16/FOXO translocation pulses correlate with a major physiological transition, namely the decision to arrest body growth or not. Periods of infrequent short pulses often coincide with growth, while long or frequent pulses coincide with growth arrest, and DAF-16/FOXO loss results in a lack of growth arrest under stress. The stochastic yet synchronized pulsing of DAF-16/FOXO under constant conditions excludes that coordination results simply from each cell responding independently to a spatially uniform stress, and instead implies active synchronization. Our findings raise urgent questions about the molecular basis of the underlying synchronizing signals. We speculate that this active mechanism of body-wide IIS synchronization is important also in humans, for growth and for other insulin-dependent processes and diseases, including diabetes, obesity, and longevity[16–19], that all hinge on tissue- or body-wide coordination.

Results

Synchronized, stochastic DAF-16/FOXO nuclear translocation pulses

We visualized DAF-16/FOXO nuclear localization using a transgenic line expressing a functional DAF-16::GFP fusion protein that tags the DAF-16a/b isoforms[33] and is a standard reporter for studying DAF-16/FOXO activation[21,34–37]. When we examined DAF-16::GFP localization in a population of L1 larvae[32] under starvation or 300 mM osmotic shock (Fig. 1B**, Methods**), DAF-16::GFP was nuclear in most animals, as expected, yet 20-40% of animals instead showed cytoplasmic localization, consistent with previous observations. Even for conditions that elicited a strong response (32 °C heat shock or *daf-2(e1368)* mutants under starvation), still 5-10% of animals did not display full nuclear localization.

So far, DAF-16::GFP nuclear localization has only been studied by comparing static snapshots of animals under normal or stressed conditions. Instead, we performed time-lapse microscopy on animals hatched from eggs placed in 0.2×0.2 mm hydrogel microchambers[38] without food, allowing us to examine starvation-induced DAF-16/FOXO translocation dynamics in individual larvae (SI Fig. 1A). Upon hatching in the absence of nutrients, DAF-16::GFP translocated from the cytoplasm to the nucleus within ~2 hr in most animals, as expected. However, DAF-16::GFP typically moved back into the cytoplasm after ~1 hr (Fig. 1C) and continued to shuttle between the nucleus and the cytoplasm in pulses with ~2 hr duration (SI Movie 1), even as starvation conditions were constant. Strikingly, even though the timing and duration of DAF-16::GFP translocation pulses varied in time, DAF-16::GFP translocation was highly synchronized between *daf-16*-expressing cells throughout the body (Fig. 1D, SI Movie 1).

We quantified DAF-16/FOXO nuclear translocation dynamics by measuring the ratio R between nuclear and cytoplasmic fluorescence (SI Fig. 1B, **Methods**). We focused on intestinal cells, that form a stereotypical array along the antero-posterior (A-P) axis spanning approximately half the body length of L1 larvae. Most animals displayed initial oscillation-like translocation pulses (Fig. 1F, G), followed by more persistent DAF-16::GFP nuclear localization ($R > 1$) as stress persisted, although brief pulses of translocation to the cytoplasm remained visible even at this stage. In general, R displayed clear variability between individual animals, in terms of both frequency and number of translocation pulses, underlining their stochastic nature. Yet, despite this individual variability, R dynamics were always strongly correlated between intestinal cells at markedly different positions along the A-P axis (Fig. 1G, H), revealing a degree of synchrony that was unexpected for an inherently stochastic process.

We found no DAF-16::GFP translocation pulses when eggs hatched in microchambers filled with plentiful food (SI Fig. 1C), indicating that they are a specific response to starvation. We observed similar synchronized nuclear translocation pulses in a strain carrying a DAF-16::GFP endogenous CRISPR/Cas9 knock-in fusion (DAF-16::GFPsc)[39] (Fig. 1E, SI Fig. 1D–F), confirming that these translocation pulses were not an artifact of the DAF-16::GFP transgenic line. Moreover, synchronized DAF-16::GFP translocation pulses were also seen in the intestine and hypodermis of young adult animals upon exhaustion of their bacterial food supply (SI Fig. 1G-I), indicating a general starvation response. Finally, we observed nuclear translocation pulses of the human DAF-16 homolog FOXO3A in human U2OS cells carrying a FOXO3A::GFP plasmid (SI Fig. 2), with pulse amplitude increasing with serum starvation (decreasing % FBS). This matches recent observation of starvation-induced FOXO1 nuclear translocation pulses[40], and shows that pulsatile regulation by FOXO TFs is likely a general feature of IIS. Overall, these measurements reveal that the animal-to-animal variability in DAF-16::GFP nuclear localization under constant stress, which was previously observed on the population level, in large part reflects stochastic DAF-16::GFP translocation pulses occurring with high internal synchrony within each individual.

Synchrony of DAF-16/FOXO translocation pulses for different stress types

We next asked if synchronized DAF-16::GFP nuclear translocation pulses were also seen for other types of stress. We exposed L1 larvae hatched in microchambers filled with food either to heat or osmotic shock (SI Fig. 3, **Methods**), which are both known to induce DAF-16 nuclear translocation[21,33]. Both stress treatments resulted in DAF-16::GFP translocation pulses but with qualitative differences in dynamics. In particular, under 200 mM NaCl osmotic shock individuals often showed short, infrequent translocation pulses that were isolated in time (Fig. 2A), while heat shock typically induced a single, transient translocation pulse immediately upon heat exposure (SI Fig. 3). Nevertheless, for both stresses the R dynamics was synchronized between intestinal cells, even for the more irregular pulses seen for animals under osmotic shock.

To put an upper bound on the degree of synchrony, we imaged DAF-16::GFP pulses with high, 30 s time resolution in animals under starvation stress and quantified R in the intestinal cells Int2-Int8 (Fig. 2B), excluding the four Int1 and two Int9 cells where DAF-16::GFP was difficult to resolve in single cells. At this increased time resolution, we could observe gradual nuclear translocation of DAF-16::GFP over a ~20 min time interval. Moreover, we found that R displayed a shift in time between different cells, although the magnitude of the shift was small compared to the timescale of translocation. To quantify the shift, we cross-correlated R between each pair of cells (Fig. 2C, SI Fig. 4A–D), where the lag time at which the cross-correlation peaked represented the delay in pulses between the two cells.

We found that cells in close physical proximity within the body, such as Int2V and Int2D that have the same A-P position, showed no delay (Fig. 2C–E). However, we found that the cross-correlation showed a peak at positive lag time when we compared anterior cells to more posterior cells (Fig. 2C), with the magnitude of the delay increasing with the distance between the cells (Fig. 2D, E). Notably, the sign of the delay indicated an anterior-to-posterior order in DAF-16::GFP pulse dynamics, that was consistent between different animals, with pulse dynamics initiating in the Int2 cells ~3 min before the Int8 cells. When analyzing high time resolution data obtained for osmotic shock, we found an equally strong synchronization, with delays between cells of <3 min (Fig. 2E). Intriguingly, the nature of the delay was more complex than the simple anterior-to-posterior order seen for starvation, and instead reflected a partial dorsal-ventral ordering. For

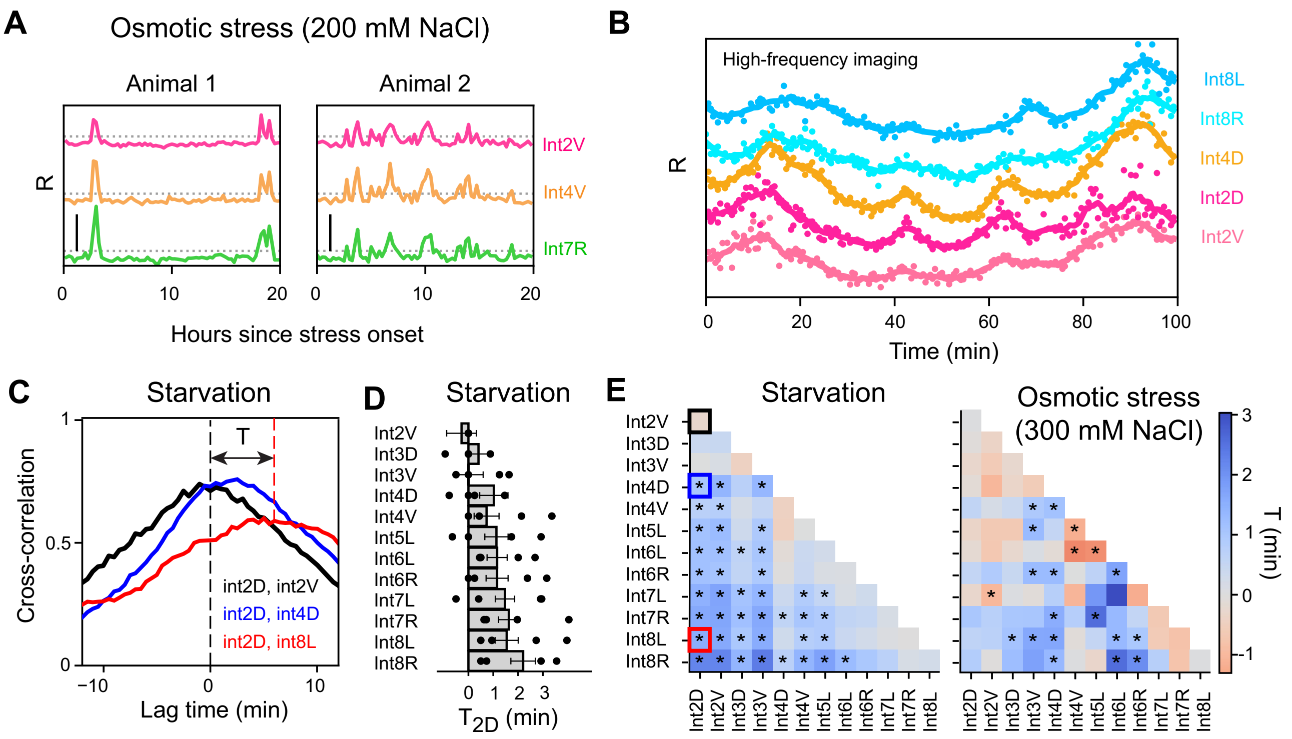

Fig. 2 | Synchrony of DAF-16/FOXO translocation dynamics in intestinal cells. **A** Synchronized DAF-16::GFP nuclear localization *R* in intestinal cells of animals exposed to 200 mM NaCl osmotic shock. Dashed lines is *R* = 1.03 for each cell. Vertical black line indicates amplitude of 0.5. **B** DAF-16::GFP nuclear localization *R* in intestinal cells of a starved L1 animal, imaged at 30-second time resolution (markers). Lines are data smoothed with a Savitzky-Golay (S-G) filter. Individual tracks are shifted along the y-axis for clarity. **C** Cross-correlation of *R* for int2D and intestinal cell pairs at the same (int2V) or increasing A-P distance (int4D and int8L, respectively). Data is for *n* = 6 animals. The lag time *T* at which the cross-correlation peaks corresponds to the average delay in *R* between cells. **D** Mean measured delay T_{2D} between Int2D and all other intestinal cells. Dots indicate data from individual animals. Error bars are 95% confidence intervals of the peak centroid distributions obtained from Monte-Carlo simulations (*n* = 4 animals). **E** Heatmap showing the delay *T* between all pairs of intestinal cells for starvation (left, *n* = 6 animals) and osmotic shock (right, *n* = 6). Squares denoted by * indicate a delay that is significantly different from 0 (Indicating that *T* = 0 lies outside the 95% confidence interval. One-sided Monte Carlo test, no adjustments for multiple comparisons). Outlined squares correspond to the curves in **C**.

example, the ventral cells Int2V, Int3V, and Int4V had pulse dynamics delayed compared to the more dorsal cells Int4D and Int5L (SI Fig. 4E, F). Overall, this suggests that the synchronizing mechanism depends at least partially on stress type.

DAF-16/FOXO translocation dynamics reflect both stress type and magnitude

We then more systematically examined the differences in DAF-16::GFP translocation dynamics between different stresses. Given the observed synchrony between different intestinal cells, we compared *R* dynamics quantified over all intestinal cells. Differences in DAF-16::GFP translocation dynamics were apparent when we compared population-averaged translocation dynamics, ⟨*R*⟩, between stresses (Fig. 3A): for 32 °C heat shock, ⟨*R*⟩ exhibited a single translocation peak ~1.5 hrs after stress onset, consistent with our observations in individuals (SI Fig. 3), followed by increasing nuclear localization as stress persisted. A similar immediate peak in ⟨*R*⟩ was visible upon starvation, but here followed by additional peaks, consistent with our earlier observation of more oscillation-like translocation pulses in individual animals (Fig. 1F, G). In contrast, no clear peaks in ⟨*R*⟩ were visible for 300 mM NaCl osmotic shock, as expected for the random translocation pulses observed in individuals (Fig. 2A).

To further differentiate *R* dynamics between starvation and osmotic shock, we determined the autocorrelation of *R* (Fig. 3B). Indeed, for starvation, the autocorrelation in individual animals was oscillatory with exponentially decreasing envelope, a signature of stochastic oscillations. The population-averaged autocorrelation decayed more rapidly, showing only two peaks, at 2 and 4.25 hr, reflecting the inherent variation in pulse dynamics between individuals. In contrast, the autocorrelation of *R* for osmotic shock showed no peaks of positive autocorrelation, both in individuals and averaged over all animals (Fig. 3B), consistent with non-oscillatory pulse dynamics. For osmotic shock, the valley of negative autocorrelation at 5 hr might reflect underlying stochastic dynamics operating close to, but still outside an oscillatory regime[41]. The *R* dynamics in individuals highlighted intrinsic variability in translocation pulse dynamics also for osmotic and heat shock (Fig. 3C, F), with extensive variability in number and duration of pulses.

In contrast to starvation, for osmotic and heat shock we could vary stress magnitude and examine the impact on DAF-16::GFP pulse dynamics. For osmotic shock, we hatched larvae in microchambers soaked with salt concentrations increasing from 200 to 400 mM NaCl. For 200 mM NaCl, we found that DAF-16::GFP displayed infrequent and short (<1 hr) pulses of nuclear localization, while increasing NaCl levels led to a concomitant increase in the fraction of time ϕ that DAF-16::GFP was nuclearly localized (Fig. 3C, SI Fig. 5). This was due mainly to an increase in pulse duration (Fig. 3D), rather than pulse frequency (SI Fig. 5), and occurred without increase in pulse amplitude (Fig. 3E), i.e. the degree of nuclear enrichment.

For heat shock, we shifted hatched L1 larvae from 20 °C to temperatures ranging from 31 °C to 33 °C. For 31 °C and 32 °C heat shocks, most animals displayed a single transient pulse of strong nuclear translocation directly after the shift to high temperature (Fig. 3F). However, both the amplitude and duration of the initial translocation pulse increased with higher temperature (Fig. 3G, SI Fig. 5). In addition, the nuclear localization pulses that followed the initial pulse increased

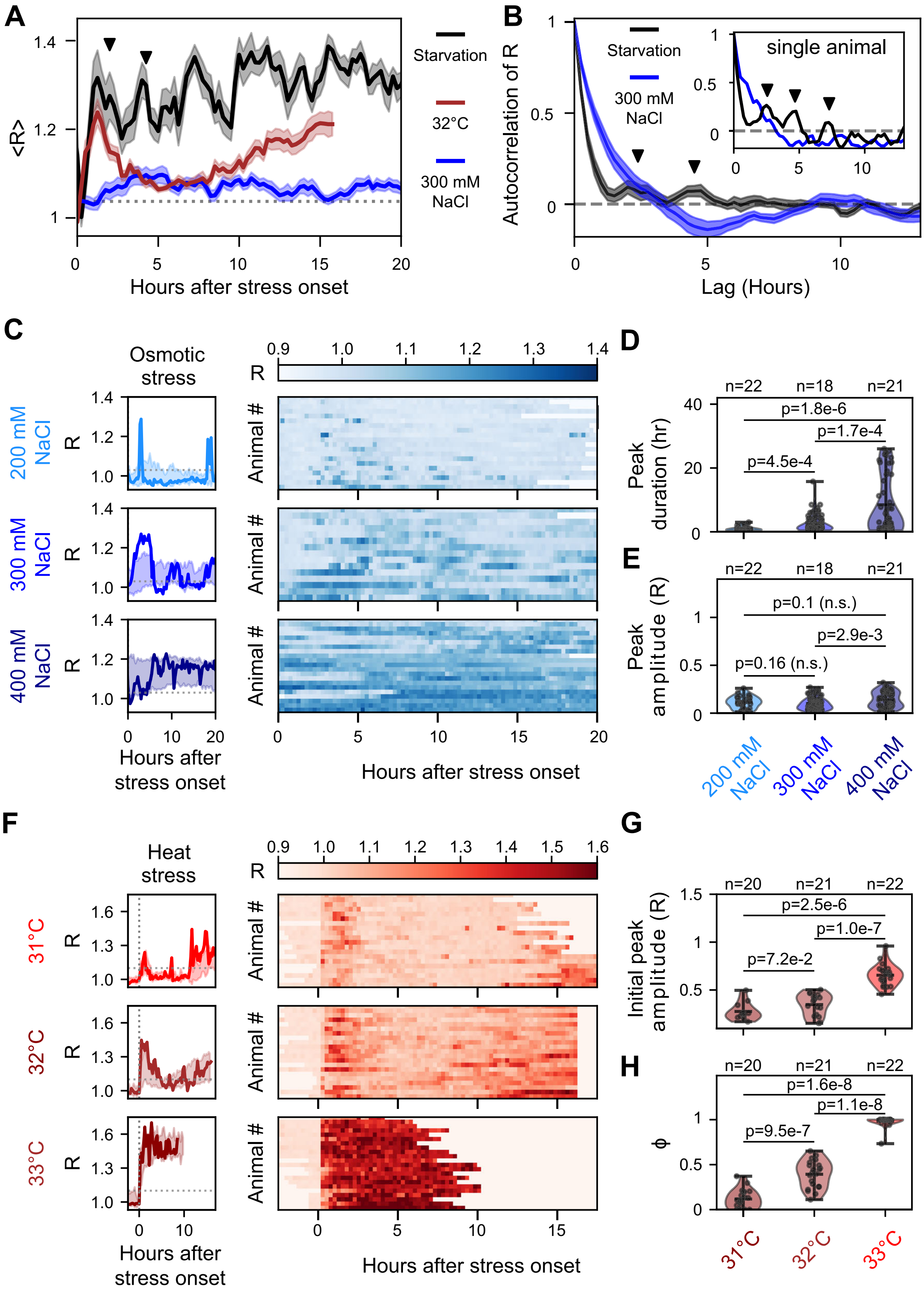

with temperature, resulting in a higher fraction of time ϕ that DAF-16::GFP was nuclear ($R > 1.05$, Fig. 3H). Following a 33 °C heat shock, in contrast, we no longer observed a transient pulse, but found that DAF-16::GFP, after translocating, remained highly enriched in the nucleus for the duration of the experiment (Fig. 3F). In conclusion, for both osmotic and heat shock, higher stress magnitude was apparent through the increased fraction of time that DAF-16::GFP was nuclear. Overall, this showed that DAF-16::GFP nuclear translocation dynamics was not only distinct for different types of stress (starvation, osmotic shock, or heat shock), but also reflected stress magnitude.

Mutations in DAF-16/FOXO regulators change translocation pulse dynamics

We next probed molecular regulation of DAF-16/FOXO translocation pulses by studying how pulse dynamics was impacted by mutations in key regulators of DAF-16/FOXO nuclear translocation. We first

Fig. 3 | DAF-16/FOXO nuclear translocation dynamics depends on stress type and magnitude. A Population-averaged nuclear localization R for starvation (black, $n = 13$), 300 mM osmotic shock (blue, $n = 18$) and 32 °C heat shock (red, $n = 21$). Error bars are S.E.M. Arrowheads indicate the population-average oscillation period of DAF-16::GFP translocated as determined in **B**. **B** Population-averaged autocorrelation of R for starvation (black, $n = 13$) and 300 mM osmotic shock (blue, $n = 18$). Inset shows autocorrelation for an individual animal. Error bars are S.E.M. Peaks in autocorrelation (indicated by arrows) correspond to oscillatory DAF-16::GFP translocation dynamics. **C** Individual tracks (left) and population view heatmaps (right) of R for increasing osmotic shock. Individual tracks (left) are shown as lines, while shaded regions indicate mean +/− standard deviation for the population. **D** Distribution of duration and **E** amplitude of DAF-16::GFP nuclear translocation pulses for osmotic shock. Increasing osmotic shock leads to more prolonged pulses without affecting amplitude. Violin plots indicate mean, min and max values, p-values are for one-sided Mann-Whitney U test, while n-values indicate animals, n.s.: not significant. **F** Same as **C**, but for increasing heat shock. For 33 °C heat shock, observation time is limited to ~10 h due to heat-induced shrinkage of the hydrogel microchambers. Distribution of amplitude of the first DAF-16::GFP translocation peak (**G**) and fraction of time ϕ that DAF-16::GFP is nuclear (**H**) for increasing heat shock. Violin plots indicate mean, min and max values. Violin plots indicate mean, min and max values, p-values are for a one-sided Mann-Whitney U test, while n-values indicate animals.

examined mutants of two core components of the IIS signal transduction pathway, *daf-2* and *akt-1* (Fig. 4A). We selected the *daf-2(e1368)* mutant that carries a mutation in the ligand-binding domain of the DAF-2 insulin receptor[42], resulting in strongly reduced IIS activity. The Akt/PKB kinases *akt-1* and *akt-2* are the core kinases that phosphorylate DAF-16/FOXO, thereby promoting its cytoplasmic localization in response to DAF-2 activation[22]. Loss of AKT-1 and AKT-2 both increased DAF-16/FOXO nuclear localization in unstressed animals, but with a stronger impact of AKT-1[43]. We therefore focused on the deletion allele *akt-1(ok525)*[44].

Importantly, both *daf-2(e1368)* and *akt-1(ok525)* mutants displayed synchronized DAF-16::GFP translocation pulses upon starvation (Fig. 4B, SI Fig. 6). For starved *daf-2(e1368)* animals, DAF-16::GFP was localized primarily in the nucleus, with infrequent ~1 hr periods of cytoplasmic localization (Fig. 4C). Consequently, *daf-2(e1368)* mutants showed increased pulse duration and fraction of time ϕ that DAF-16::GFP was nuclear (Fig. 4D, SI Fig. 6), consistent with population-level measurements (Fig. 1B). The prolonged nuclear localization in *daf-2(e1368)* mutants resembled that of wild-type animals when oscillations cease after prolonged starvation (>10 hr, Fig. 1F), suggesting that the latter originates from a decrease of IIS activation over time. In starved *akt-1(ok525)* animals, DAF-16::GFP nuclear localization during pulse maxima was comparable to wild-type, resulting in the same overall amplitude distribution, yet pulse minima were substantially increased, leading to higher apparent pulse duration and ϕ (Fig. 4C, D, SI Fig. 6C, D). In particular, during pulse minima, we rarely observed lower DAF-16::GFP fluorescence intensity inside the nucleus compared to the cytoplasm (SI Fig. 6E). Overall, this increased DAF-16::GFP nuclear localization was consistent with the expected impact of decreased Akt kinase activity. We probed this further by instead increasing *akt-1* activity, using the *pptr-1(tm3103)* mutant[45]. PPTR-1 inhibits the activity of AKT-1 (Fig. 4A), but not AKT-2, with PPTR-1 loss leading to decreased DAF-16/FOXO nuclear localization[46]. Starved *pptr-1(tm3103)* mutants also showed synchronized DAF-16/FOXO translocation pulses (Fig. 4B, SI Fig. 6A), but with decreased pulse duration and ϕ compared to both wild-type and *akt-1(ok525)* animals (Fig. 4C, D, SI Fig. 6BA). Interestingly, *pptr-1(tm3103)* mutants also showed lower peak maxima and, hence, a significant reduction in pulse amplitude (Fig. 4C,D). Together, this indicate that Akt kinase activity controls the bias between nuclear and cytoplasmic localization of DAF-16/FOXO pulses, impacting both their duration and amplitude.

DAF-16/FOXO is phosphorylated also by kinases outside of the IIS pathway, such as AMP-activated kinase (AMPK)[47]. AMPK senses AMP:ATP ratio and is activated by decreased energy levels, suggesting a role as a nutrient sensor. Indeed, AMPK mutants fail to enter L1 arrest upon starvation[20], while AMPK increases longevity upon dietary restriction in a DAF-16/FOXO-dependent manner[47]. However, it is an open question whether AMPK directly regulates DAF-16/FOXO nuclear localization. We therefore examined DAF-16/FOXO pulse dynamics in *aak-1(tm1944);aak-2(gt33)* mutants, where two AMPK subunits *aak-1* and *aak-2* are deleted, as this showed greater sensitivity to stress than single *aak-1* or *aak-2* mutants[48]. Most *aak-1(tm1944);aak-2(gt33)* embryos obtained by bleaching adults, to ensure that they were not contaminated with remaining *E. coli* food, died before hatching, likely due to increased stress sensitivity. We therefore followed an alternative approach, letting embryos hatch with a limited *E. coli* supply, that was depleted ~5 hr after hatching (SI Fig. 6F). For wild-type DAF-16::GFP animals, food depletion resulted in DAF-16/FOXO translocation pulses similar to full starvation, but with lower duration (Fig. 4E, F, SI Fig. 6B). Notably, *aak-1(tm1944);aak-2(gt33)* animals still showed synchronized DAF-16/FOXO translocation pulses upon food depletion (Fig. 4B, E), but with markedly reduced duration and amplitude (Fig. 4F), demonstrating that AMPK increased DAF-16/FOXO nuclear localization upon starvation. Given the link between AMPK and nutrient depletion, we wondered whether AMPK loss might have a weaker impact on DAF-16/FOXO pulse dynamics for stresses that do not involve nutrient depletion, such as osmotic shock. Indeed, for *aak-1(tm1944);aak-2(gt33)* animals exposed to 300 mM NaCl, we found no changes to pulse duration and fraction of time ϕ that DAF-16/FOXO was nuclear, although we did observe differences in amplitude and frequency (Fig. 4F, SI Fig. 6B).

Overall, the IIS and AMPK mutants we tested still exhibited synchronized DAF-16/FOXO translocation pulses, indicating that pulses arise through more complex mechanisms. However, our results revealed that characteristics of stress-induced DAF-16/FOXO pulses, such as duration, frequency and amplitude, are controlled by IIS components and AMPK signaling.

DAF-16/FOXO pulses correlate with arrest of body growth

We then examined possible functional roles of DAF-16/FOXO translocation pulses, focusing on the most prominent feature of L1 arrest, namely arrest of body growth[7,20]. IIS and DAF-16/FOXO have a well-established role in promoting starvation-induced cell cycle arrest in a broad range of tissues, both during L1 arrest and in other late-larval checkpoints[20,49,50]. However, this by itself does not explain growth arrest, as body growth in larvae is primarily driven by cell volume growth, rather than cell proliferation[51]. Also, growth arrest does not simply reflect a lack of food, as it is observed also for stresses such as heat or osmotic shock, where sufficient food is present to support growth[21,52]. We therefore examined if body growth itself was also actively regulated by IIS and DAF-16/FOXO.

As a measure of body growth, we quantified the length of animals along their A-P axis as a function of time, for unstressed and different stressed conditions. In the absence of stress, body length increased approximately linearly over the course of the L1 larval stage, as described previously[38,53,54], but such extension was absent upon starvation (SI Fig. 7A, B). While body growth was similarly arrested for 300 mM NaCl osmotic shock (SI Fig. 7C), we observed a surprising variability in growth arrest for 200 mM NaCl (Fig. 5A): some animals showed fully linear growth, albeit at lower rate than without stress, while others displayed intermediate growth or full arrest. Inspecting individual animals indicated that periods of low growth coincided with sufficiently long or frequent DAF-16::GFP pulses (Fig. 5A), suggesting a link between DAF-16::GFP translocation and body growth. To study this further, we compared each animal's average growth rate to the fraction of time ϕ that DAF-16::GFP was nuclear (Fig. 5B). For 200 mM NaCl,

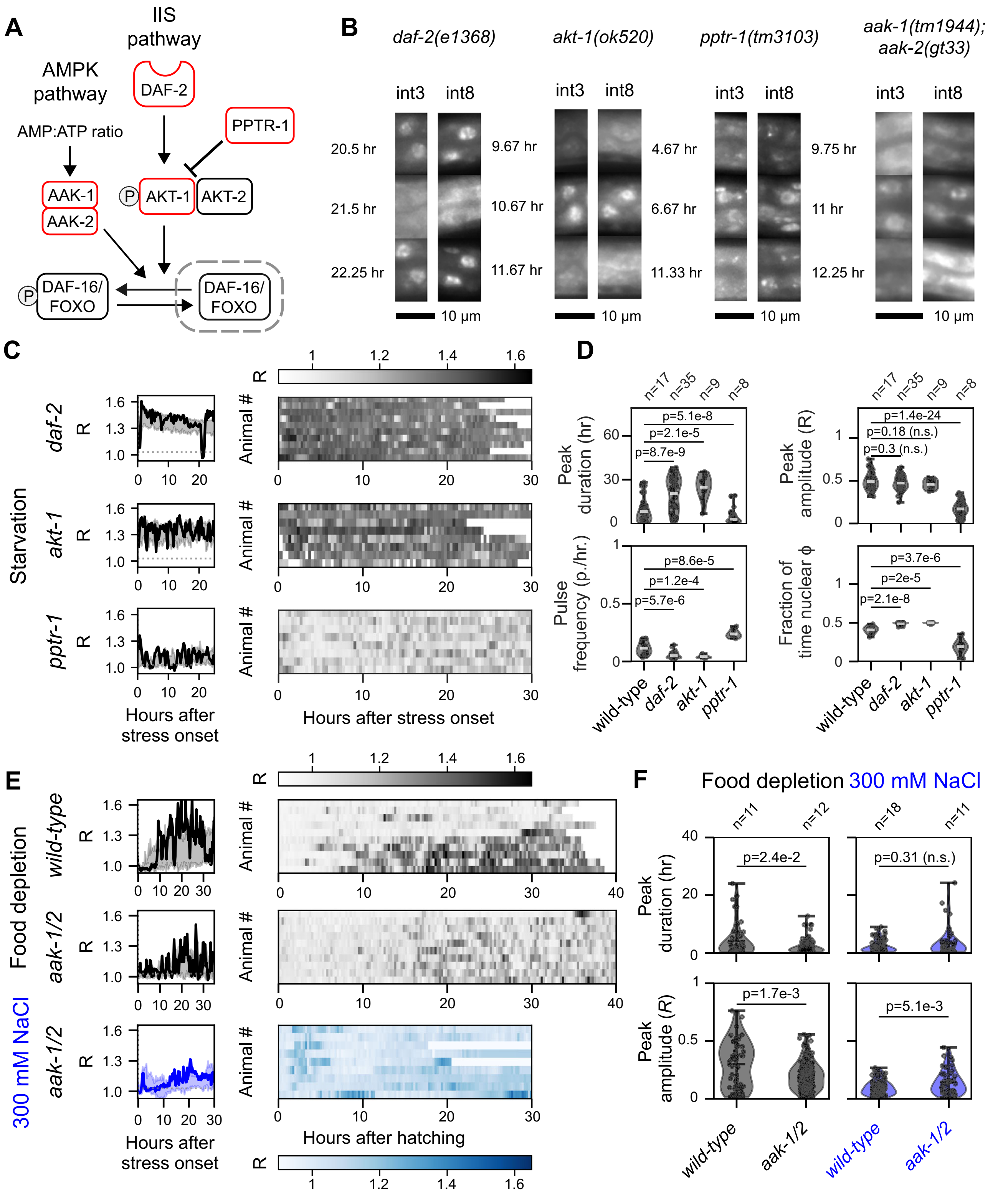

growth rate and ϕ showed a strong correlation (Pearson $r = -0.9$, $p = 3e-7$), with individuals with high ϕ generally showing less growth. For higher osmotic shock, where growth was severely reduced for all individuals, we found either a similar, but weaker correlation (250 mM NaCl, $r = -0.7$, $p = 1e-2$) or no clear correlation (300 mM NaCl). We note that for 250 and 300 mM NaCl, animals often showed a negative growth rate, likely reflecting a reduction in body volume due to osmotic pressure[55], independent of growth arrest. To examine whether DAF-16::GFP translocation coincided with growth arrest in time, we measured growth rate and ϕ over 5 hr time windows (Fig. 5C), corresponding roughly to the timescale of a translocation pulse. Indeed, growth rate and ϕ were also correlated on this time scale ($r < -0.4$, $p < 4e-2$), with some individuals showing clear halting and resumption of growth as ϕ changed between time windows (Fig. 5C, SI Fig. 7D,E).

We then tested if growth depended in a simple, direct manner on DAF-16::GFP nuclear localization. We found that *daf-2(e1368)* mutants on 200 mM NaCl showed a strongly increased pulse amplitude and duration, consistent with their reduced activation of IIS or

Fig. 4 | Mutations in DAF-16/FOXO regulators change translocation pulse dynamics. **A** Overview of key DAF-16/FOXO regulators, with mutants studied indicated in red. **B** DAF-16::GFP nuclear translocation dynamics in intestinal cells int3 and int8 upon starvation stress. For all DAF-16/FOXO regulator mutants, nuclear translocation pulses were synchronized between int3 and int8. Scale bar: 10 μm. **C** Individual tracks (left) and population heatmaps (right) of R for IIS pathway mutants *daf-2*, *akt-1* and *pptr-1* under starvation. Shaded region (left) indicates mean +/- standard deviation for all animals. Data for *akt-1* mutants was obtained by manual analysis, while other mutants were analyzed automatically based on the intestinal nuclear reporter. **D** Distribution of pulse duration, frequency, amplitude, and fraction of time ϕ that DAF-16/FOXO was nuclear, compared for wild-type animals and mutants in **C**. Violin plots indicate mean, min, and max values, p-values are for a one-sided Mann-Whitney U test, while n-values indicate animals, n.s.: not significant. **E** Individual tracks (left) and population heatmaps (right) of R for AMPK signaling mutant *aak-1;aak-2* under starvation by food depletion and under 300 mM NaCl osmotic shock. Shaded region (left) indicates mean +/- standard deviation for all animals. Food was depleted at ~5 hr after hatching, and the wild-type response to food depletion is shown as a comparison. **F** Distribution of pulse duration and frequency, compared for wild-type and *aak-1;aak-2* animals under starvation by food depletion (left) or NaCl osmotic shock (right). Violin plots indicate mean, min and max values, p-values are for one-sided Mann-Whitney U test, while n-values indicate animals.

hyperactivation of DAF-16/FOXO, reflected in higher average ϕ (Fig. 5D, SI Fig. 8A). At the same time, they showed similar individual variability as in wild-type animals, with some individuals exhibiting few, short pulses, while others had persistently nuclear DAF-16::GFP. Moreover, we found a similar correlation between ϕ and growth rate (Fig. 5E, $r = -0.9$, $p = 3e{-4}$). However, despite higher average ϕ, *daf-2* mutants did not show higher fraction of growth arrest (SI Fig. 8B). Indeed, *daf-2* mutants exhibited the same decrease in growth rate only at substantially higher ϕ compared to wild-type animals (Fig. 5E), with a similar difference seen when comparing pulse amplitude instead of ϕ (SI Fig. 8C). However, *daf-2* mutants hatched at larger body size than wild-type animals (SI Figure. 8D), suggesting that *daf-2* and wild-type animals already differ at hatching and might therefore also differ in response to external stress. Overall, these results showed that growth arrest did not depend simply on the level or duration of DAF-16::GFP nuclear presence, and leave open the possibility that it depends on more complex features of translocation pulse dynamics.

The coincidence of DAF-16::GFP nuclear translocation pulses and growth arrest (Fig. 5C) suggested that both are linked. However, the observation that increased DAF-16::GFP nuclear localization in *daf-2* mutants did not further increase the degree of growth arrest (Fig. 5E) indicated that growth arrest might not depend on DAF-16/FOXO. In this scenario, DAF-16::GFP nuclear translocation and growth arrest would be controlled independently and in parallel by an upstream stress signal. To test whether the observed growth arrest is DAF-16/FOXO-dependent, we placed animals carrying a *daf-16(mu86)* null allele under the same stress conditions. We found that *daf-16(mu86)* animals exposed to osmotic shock (250 or 300 mM NaCl) showed significantly higher growth than wild-type animals, which typically showed full growth arrest under these conditions (Fig. 5G, H). We found that heat stress also induced growth arrest, with higher temperature corresponding both to more prolonged DAF-16/FOXO nuclear localization and growth arrest (Fig. 5F, SI Fig. 7F). Moreover, even for 33 °C heat stress, corresponding to the strongest arrest, continued growth was still seen in *daf-16(mu86)* mutants (Fig. 5G, H). Growth rates in *daf-16(mu86)* mutants under stress remained lower than under unstressed conditions, which was partially explained by stressed *daf-16(mu86)* larvae still showing an initial arrest period, before resuming growth (Fig. 5H). This might simply reflect the difficulty of body growth under stress conditions, but could also indicate that the impact of DAF-16/FOXO translocation on growth arrest is more indirect, acting on longer timescales than that of the DAF-16/FOXO translocation pulses.

Impact of stress dynamics on DAF-16 translocation and target gene expression

So far, we have examined DAF-16/FOXO translocation in response to constant stress. Using our ability to control temperature with high time resolution, we exposed DAF-16::GFP animals to alternating intervals of 20 °C and 33 °C heat stress, of varying number and duration (Fig. 6A). We found that DAF-16::GFP translocation closely followed heat intervals, with shifts to 33 °C resulting in rapid DAF-16::GFP nuclear localization and cytoplasmic localization upon shifting back to 20 °C (Fig. 6B,C, SI Fig. 9A), with similar results also for 32 °C heat intervals (SI Fig. 9B). However, we observed in some individuals that DAF-16:GFP translocation continued for 2 pulses at 20 °C, after 33 °C heat intervals ended (Fig. 6D). Such additional DAF-16::GFP translocation pulses were seen following 8 × 0.75 hr 33 °C + 1 hr 20 °C intervals (2/12 animals), but not for 4×1 hr 33 °C + 1.5 hr 20 °C intervals (0/11 animals, SI Fig. 9C). Such occurrence of additional translocation pulses following periodic forcing by heat intervals is reminiscent of similar behavior in excitable systems[56] and might thus provide insight into their underlying mechanism.

DAF-16/FOXO mediates stress response primarily by binding target gene promotors to upregulate their expression[29,30,57], which thus crucially depends on DAF-16/FOXO nuclear localization. Given that different heat treatments caused different DAF-16::GFP translocation dynamics, we therefore wondered if they also differed in impact on DAF-16/FOXO target gene expression. We focused on the DAF-16/FOXO target *sod-3*, a superoxide dismutase expressed upon oxidative stress[58], using a SOD-3::GFP translational reporter[59]. While no SOD-3::GFP was induced at 20 °C (Fig. 6E), as expected, induction was observed at constant 33 °C heat shock (Fig. 6F, I, SI Fig. 9D), a condition that caused constant nuclear localization in DAF-16::GFP animals (Fig. 3F). We then compared the SOD-3::GFP level induced by the same total heat stress (8 hr at 33 °C) but now delivered in different heat interval treatments. Interestingly, 4×2 hr 33 °C + 3 hr 20 °C intervals induced higher SOD-3::GFP level (Fig. 6G, I), even as heat stress intensity decreased, as heat was now interspersed with 20 °C intervals. Even higher SOD-3::GFP level was induced by 8×1 hr 33 °C + 1.5 hr 20 °C intervals (Fig. 6H, I), corresponding to the same heat stress intensity but delivered in shorter intervals. Further decreasing heat stress intensity, by applying 8×1 hr 33 °C + 2 hr 20 °C intervals, reduced SOD-3::GFP (Fig. 6I). Heat-pulse induction of SOD-3::GFP depended on DAF-16/FOXO, as SOD-3::GFP was not induced in *daf-16(mu86);sod-3::GFP* animals (Fig. 6H, I). A transcriptional reporter for the DAF-16/FOXO target *hsp-16.2*[60,61], a heat shock protein, showed a similar increase in induction with shorter 33 °C pulses (Fig. 6I, SI Fig. 9E). SOD-3::GFP levels for the different heat treatments approached similar levels when total time of 33 °C heat stress increased, indicating that heat intervals impacted the speed of induction rather than its steady state level, yet periodic heat intervals always induced higher SOD-3::GFP than the same total duration of constant 33 °C (SI Fig. 9F).

These observations left open whether the dependence of DAF-16/FOXO target gene expression on heat stress treatment reflected changes in underlying DAF-16/FOXO translocation dynamics, or also the more general impact of the temperature changes. To probe this, we examined the impact of different heat treatments on expression of *eft-3*, a constitutively expressed housekeeping gene that is not a DAF-16/FOXO target. Here, expression of an *eft-3p::GFP* reporter[62] increased during larval development at 20 °C (Fig. 6I, SI Fig. 9D, G). Heat intervals of 8 × 1 hr 33 °C + 1.5 hr 20 °C reduced *eft-3p::GFP* expression, with further reduction for constant 33 °C (Fig. 6I, SI Fig. 9G), indicating that increased heat stress intensity lowered constitutive gene expression levels. Together, this suggested that heat-induced DAF-16/FOXO target gene expression reflected a trade-off, with higher temperature

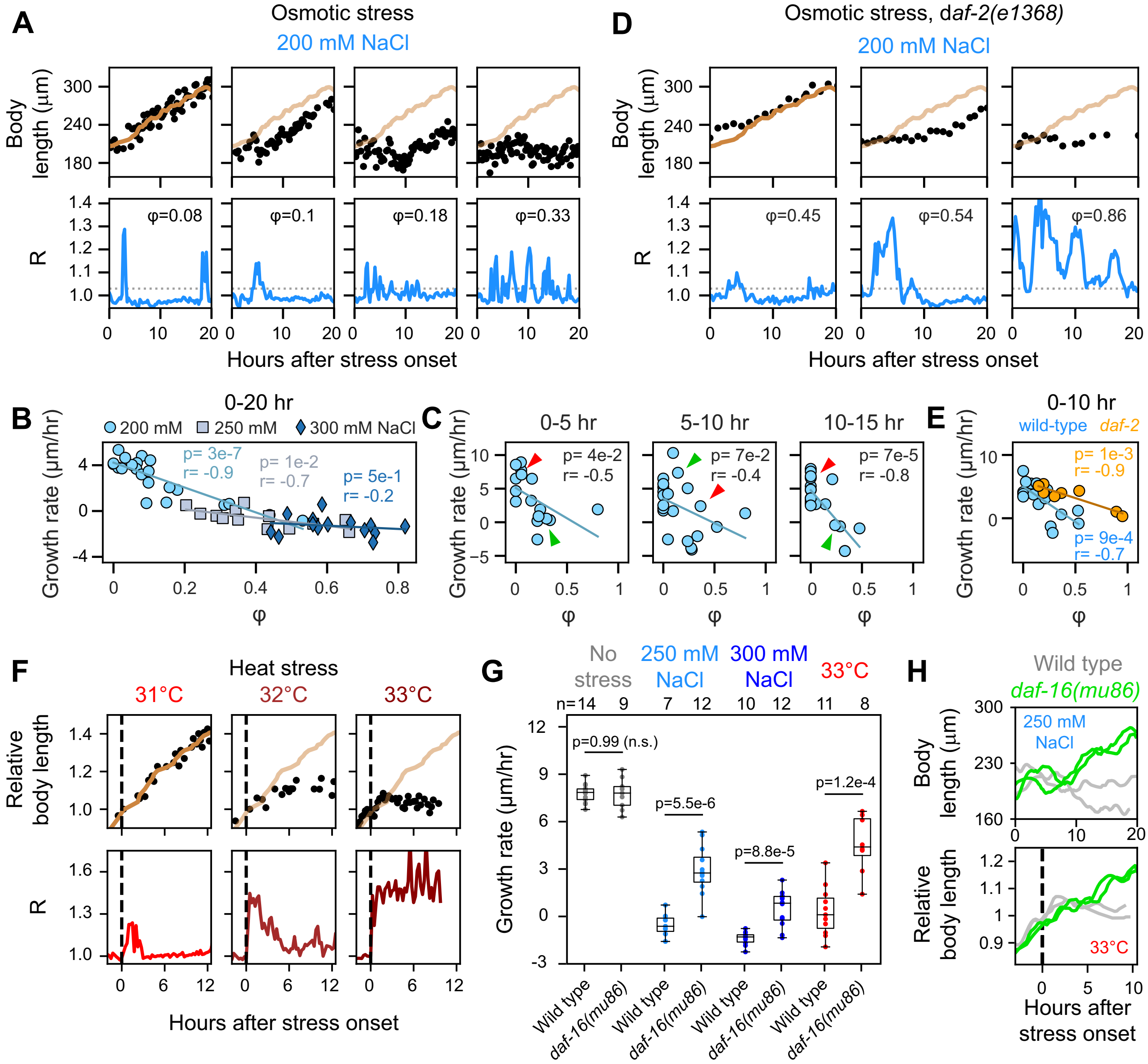

Fig. 5 | DAF-16/FOXO translocation pulses correlated with arrest of body growth. **A** Body length (top) and DAF-16::GFP nuclear localization (R, bottom) for individual animals under 200 mM NaCl osmotic shock, for increasing fractions of time ϕ that DAF-16::GFP was nuclear, defined as $R > 1.03$. Black markers are individual measurements. The orange line is length data for the animal with ϕ=0.08 smoothed with an S-G filter, shown for comparison. **B** Growth rate as a function of ϕ for different magnitudes of osmotic shock. Growth rate is defined as $\Delta L/\Delta T$, where ΔL is the change in body length over the indicated time interval ΔT. Each marker represents an individual animal. Lines are linear regression fits to each osmotic shock condition, with the corresponding Pearson correlation coefficient r and p-value (two-sided Wald test) indicated. **C** Growth rate versus ϕ for subsequent 5-hour time windows. Red and green arrows indicate two individuals that shift between periods of growth and arrest and that coincide with changes in ϕ. Pearson correlation coefficient r and p-value (two-sided Wald test) are indicated. **D** Body length and R for *daf-2(e1368)* animals under 200 mM NaCl osmotic shock. The orange line corresponds to the animal with ϕ=0.08 in **A**. **E** Growth rate versus ϕ compared between wild-type (blue) and *daf-2(e1368)* animals (orange). Lines are linear regression fits, with corresponding Pearson r and p-value (two-sided Wald test) indicated. **F** Body length and R for individuals under increasing heat shock. The dashed line is the time of the temperature shift. Body length is measured relative to length at time of heat shock, which in each individual occurs at a different time relative to hatching. **G** Comparing growth rate for wild-type and *daf-16(mu86)* animals under various stress conditions. *daf-16(mu86)* mutants sustain growth under all stress conditions, meaning that DAF-16 is required for reduced or arrested growth under osmotic shock or heat shock. Boxplots depict median and interquartile range, whiskers indicate 1.5× interquartile range, p-values are for one-sided Welch's t-test, while n-values indicate animals, n.s.: not significant. **H** Body length for two wild-type (grey) and two *daf-16(mu86)* animals (green) exposed to 250 mM NaCl (top) and 33 °C (bottom).

increasing induction by DAF-16/FOXO while simultaneously decreasing gene expression rates more generally, potentially reflecting inherent challenges of maintaining transcription under stress. This could explain our counterintuitive observation that the highest induction of DAF-16/FOXO targets occurred under pulsatile rather than constant heat stress, even though heat stress intensity was highest for the latter.

Discussion

Upon unfavorable conditions, FOXO TFs, including DAF-16/FOXO in *C. elegans*, move from the cytoplasm to the nucleus, where they induce stress resistance genes and inhibit genes for proliferation and growth[10,20,33,63,64]. The dynamics of FOXO nuclear translocation, however, remain poorly studied. Here, our dynamic measurements of DAF-16/FOXO translocation in *C. elegans* animals during stress-induced L1

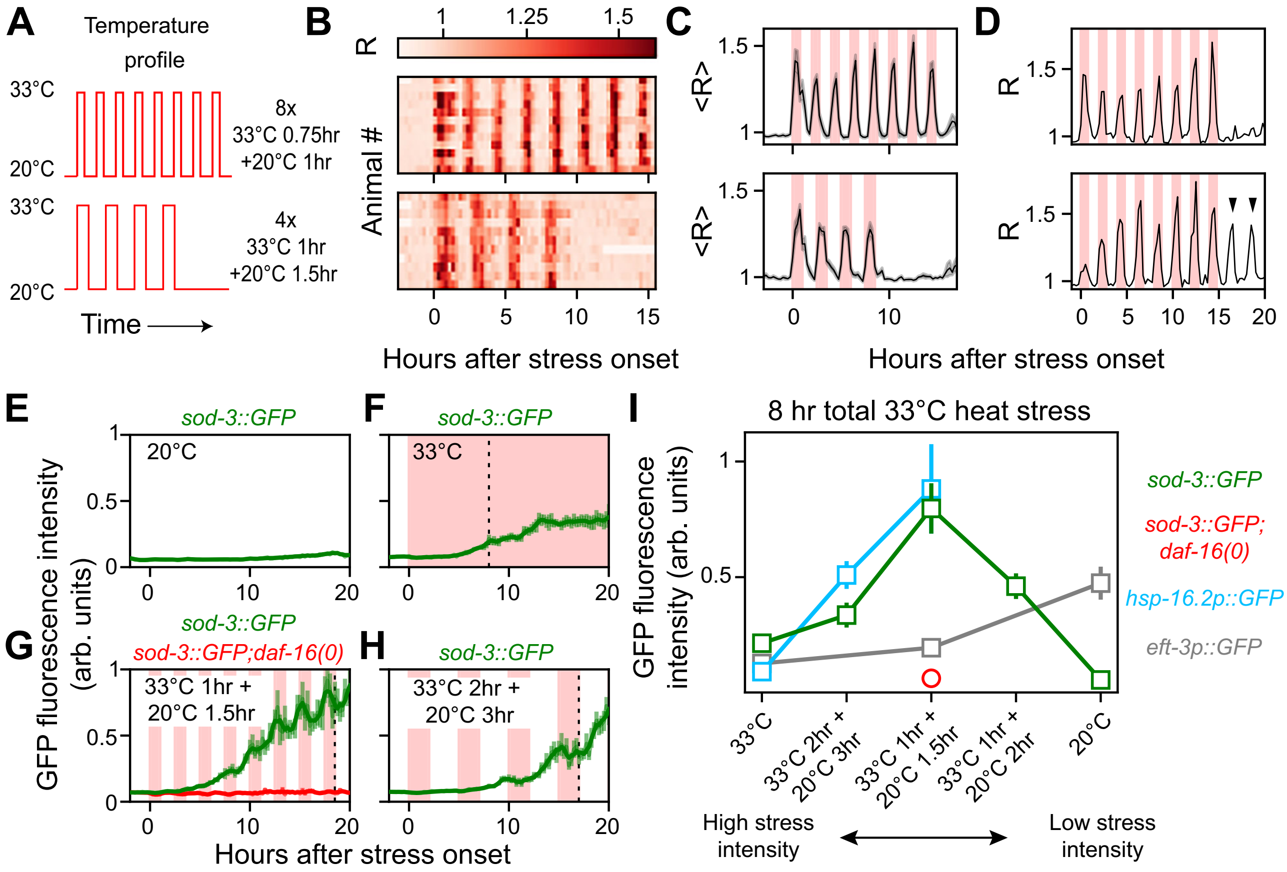

Fig. 6 | DAF-16/FOXO translocation dynamics and target gene expression for pulsatile heat stress. A Overview of pulsatile heat shock treatments. **B** Population heatmaps and **C** population-averaged tracks of DAF-16/FOXO nuclear localization *R*, for the two heat shock treatments in **A**. Time is relative to start of heat shock treatment, which was started at approximately the same time in early L1 for all animals. In **C**, heat shock intervals are indicated in red, while error bars are S.E.M. Data correspond to $n = 12$ (top) and $n = 11$ animals (bottom). **D** Tracks of *R* for two individuals for the 8x heat pulse treatment. Arrows indicate additional DAF-16/FOXO translocation pulses in one individual (bottom). **E**–**H** Fluorescence intensity of a translational reporter for the DAF-16/FOXO target *sod-3*. Fluorescence intensity is calculated as the average of the 25% brightest pixels inside the animal's body. Data is shown for **E** no heat shock, **F** constant heat shock, **G** 8×1 hr heat pulses and **H** 4×2 hr heat pulses. Dashed line in **F**–**H** indicates the time at which animals experienced 8 hr total heat shock duration. For **G**, *sod-3::gfp* expression is compared between wild-type (green) and *daf-16(mu86)* animals (red). Error bars are S.E.M. **I** Average fluorescence intensity of reporters for DAF-16/FOXO targets *sod-3* and *hsp-16.2*. Averages are shown for no stress (20 °C), and for 8-hour total heat stress (33 °C), for different heat stress treatments. As comparison, average intensity is shown for a reporter for *eft-3*, a constitutively-expressed gene that is not a DAF-16/FOXO target. Error bars are S.E.M. For heat stress treatments ranging from high to low stress intensity, averages are over $n = 10, 12, 13, 14$, and 13 (*sod-3::GFP*), $n = 4$ (*sod-3::GFP;daf-16*), $n = 13, 11$ and 8 (*hsp-16.2p::GFP*), and $n = 7, 6$ and 10 (*eft-3p::GFP*) animals.

arrest revealed that under constant stress (starvation, osmotic shock or heat), DAF-16/FOXO entered and exited the nucleus in distinct pulses (Fig. 1). Moreover, while these translocation pulses were inherently stochastic, with the incidence of an individual pulse typically difficult to predict, they were highly synchronized between the different cells in the body (Figs. 1, 2). Such tight body-wide synchronization is striking, as recent in vivo studies of pulsatile signaling, in this case of ERK activity, showed either wave-like[65] or uncoordinated dynamics[66]. We observed similar translocation pulses of FOXO3A in a human cell line following serum starvation (SI Fig. 2), mirroring recent observations of translocation pulses in human FOXO1[40], indicating that such pulses are a general feature of FOXO TFs.

Our results linked DAF-16/FOXO translocation pulses to growth arrest (Fig. 5). Both in wild-type and *daf-2* animals under osmotic shock, individuals with more DAF-16/FOXO pulses exhibited lower growth, while DAF-16/FOXO pulses coincided in time with growth arrest, even in animals that shifted between periods of arrest and growth. Under osmotic and heat stress, *daf-16(0)* mutants failed to arrest and continued growth, albeit with a delay and a reduced rate, indicating that growth arrest depended on DAF-16/FOXO action, either directly or indirectly. So far a role of DAF-16/FOXO in developmental arrest was established only for the inhibition of cell cycles[20,49,50] rather than of cell volume increase, which is the main driver of body growth[51]. Our finding that DAF-16/FOXO links to the growth of *C. elegans* larvae aligns with earlier results that *Drosophila* IIS regulates organ and cell size[3,67–70]. However, increased DAF-16/FOXO nuclear localization in *daf-2* mutants, both in level and duration, was not sufficient to increase the degree of growth arrest. This suggested that, rather than DAF-16/FOXO nuclear presence by itself, it might be more complex features of DAF-16/FOXO translocation, IIS dynamics or interaction with other proteins that determine growth arrest. Lastly, we note that a potential causative link between DAF-16/FOXO translocation and cell growth might provide a rationale for their observed synchrony, as maintaining uniform body proportions would require tight synchronization of IIS and growth state between all cells.

Our observations raise the question of how DAF-16/FOXO nuclear translocation pulses are generated, and their body-wide synchrony maintained. Mutants that impact DAF-16/FOXO phosphorylation, both of the insulin receptor *daf-2* and the DAF-16/FOXO kinase *akt-1*, perturbed DAF-16/FOXO translocation dynamics (Fig. 4), both in terms of pulse duration and amplitude. At the same time, these mutants all exhibited synchronized translocation pulses. This might reflect that these mutants were not completely null (*daf-2*), or concern proteins that function redundantly (*akt-1*), but at least indicates that precise regulation of IIS level or DAF-16/FOXO phosphorylation is not required for generating translocation pulses, nor for their body-wide synchrony. Our measurements indicate that any synchronization mechanism must be rapid, as delays in translocation between intestinal cells were of order 1–3 min (Fig. 2), much shorter than the ~20 min required for DAF-16/FOXO to transition between cytoplasmic and nuclear. For starvation, DAF-16/FOXO translocation occurred slightly earlier in anterior versus posterior intestinal cells, suggestive of a head-to-tail signal and consistent with proposed long-range signals from head neurons that detect starvation[71]. However, synchronization can also arise without long-range signals, purely through local coupling between cells[72]. In either scenario, a possible candidate for such a synchronizing signal are the insulin-like peptides (ILPs), which function as either IIS agonists or antagonists[73], and are excreted by multiple tissues, including neurons, intestine and hypodermis[22]. DAF-16/FOXO activation by IIS in one tissue induced ILP expression that impacted IIS in other tissues[74,75], showing complex inter-tissue signaling that might aid synchrony, although the large number of *C. elegans* ILPs[40] might pose a challenge in dissecting a possible role in translocation pulse synchronization.

Individual FOXO family members respond to multiple stresses by inducing stress-specific gene-expression programs[10–12,63]. In *C. elegans*, most genes expressed under osmotic shock were not induced under starvation[21], even though expression of both is mediated by IIS and DAF-16/FOXO. How the IIS pathway responds to different stresses with a tailored gene expression response is an important, unresolved question. Stress-specificity of FOXO-induced gene expression was speculated to occur through interaction with other TFs[22,63,76,77], including, for example, the proposed role for the *C. elegans* TFs HSF-1 and HCF-1 in either heat-shock or oxidative stress-specific gene expression[60,78]. Our observation that DAF-16/FOXO translocation dynamics differed qualitatively between stress types (Fig. 3) suggests an additional mechanism. Given that DAF-16/FOXO only induces gene expression while in the nucleus, different durations or frequency of DAF-16/FOXO translocation pulses therefore likely impact gene expression. Indeed, pulsatile TF translocation dynamics is found more broadly in stress response pathways[79,80], with single-cell studies demonstrating that stress-specific differences in translocation dynamics are sufficient to induce expression of different genes[80–84]. Here, by applying not constant heat, but instead periodic heat intervals, with each heat interval inducing DAF-16/FOXO translocation, we found that expression of DAF-16/FOXO target genes *sod-3* and *hsp-16.2* depended on the timing of the heat intervals, not on the total duration of applied heat (Fig. 6). While our evidence suggests that this reflected in part a broader response of gene expression to dynamic heat stress, and thus might not fully reflect the impact of DAF-16/FOXO dynamics under constant stress, it at least underscores that stress response depends on stress dynamics, not just average stress levels. Finally, we made the interesting observation that DAF-16/FOXO translocation dynamics were changed in the AMPK mutant *aak-1;aak-2* (Fig. 4). The AMPK pathway is activated by AMP:ATP ratio, acting as a cell-intrinsic nutrient sensor, rather than responding to external IIS, but impacts DAF-16/FOXO phosphorylation[22]. Hence, crosstalk of IIS and other stress-dependent pathways, such as AMPK, converging on DAF-16/FOXO might provide a mechanism to generate stress-dependent translocation pulse dynamics. Indeed, loss of AMPK signaling more strongly impacts DAF-16/FOXO translocation dynamics for starvation rather than osmotic shock (Fig. 4).

The molecular machinery of IIS is maintained throughout the animal kingdom, with a conserved role in organizing body-wide responses. Our work here highlights FOXO nuclear translocation pulses as an integral feature of IIS conserved from *C. elegans* to mammals. It will thus be important to establish whether the key features of these translocation pulses observed here, including their body-wide synchronization, stress-specificity and link to body growth, also function in higher organisms.

Methods

C. elegans Strains

Most strains were maintained on NGM seeded with OP50 at 20 °C, only animals containing *daf-2(e1368)* were kept at 15 °C. TJ356 *zIs356 [daf-16p::daf-16a/b::GFP + rol-6(su1006)]*, RW10131 *unc-119(ed3), zuIs178, stIs10024, stIs10131 [elt-7::H1-wCherry + unc-119(+)]*, DR1572 *daf-2(e1368)*, CF1038 *daf-16(mu86)*, OH16024 *daf-16(ot971[daf-16::GFP])*, RB759 *akt-1(ok525)*, JH2787 *pptr-1(tm3103)*, NB245 *aak-1(tm1944);aak-2(gt33)*, KN259 *huIs33 [sod-3::GFP + rol-6(su1006)]*, KN478 *daf-16(mu86); huIs33*, CL2070 *dvIs70 [hsp-16.2p::GFP + rol-6(su1006)]*, and EG6070 *oxSi221 [eft-3p::GFP + Cbr-unc-119(+)]* were obtained from the Caenorhabditis Genetics Center (CGC). Several lines were created by crossing: MOL193 *zIs356 [daf-16p::daf-16a/b::GFP + rol-6(su1006)], stIs10131 [elt-7::H1-wCherry + unc-119(+)]*, JVZ139 *daf-16(ot971[daf-16::GFP]), stIs10131 [elt-7::H1-wCherry + unc-119(+)]* and MOL232 *daf-2(e1368), zIs356 [daf-16p::daf-16a/b::GFP + rol-6(su1006)], stIs10131 [elt-7::H1-wCherry + unc-119(+)]*. All experiments were performed on *C. elegans* hermaphrodites.

DAF-16/FOXO localization in populations

We obtained embryos by hypochlorite treatment. For starvation, we resuspended them at 20 embryos/µl in M9 buffer. For osmotic shock, we resuspended embryos in M9 containing 10 g/l OP50-1 or in M9 containing 10 g/l OP50-1 and 300 mM NaCl. In both cases, we assessed the subcellular localization of DAF-16 after 24 hours. For heat stress, we resuspended the embryos in M9 containing 10 g/l OP50-1 and incubated them at 20 °C. After 15 hours, we split the samples into two, maintaining one at 20 °C and exposing the other at 32 °C, and measured the localization of DAF-16 after 30 min. All samples were kept rotating until the analysis of DAF-16 localization. Hatching occurs approximately 12 hours after embryo isolation, so the stage assessed is early L1. To assess DAF-16 subcellular localization, we took an 18 µl aliquot of the suspension and placed it on a microscope slide with 2 µl of 10 mM Levamisole. We used a reduced concentration of Levamisole to avoid artifactual translocation of DAF-16. The three different categories of DAF-16 localization (nuclear, intermediate, cytoplasmic) were scored visually, as described previously[32].

Microchamber preparation

Microfabricated arrays of chambers were made from epoxy master molds, that were created using standard soft-lithography techniques, as described in ref. 38. To create polyacrylamide microchamber arrays, a 10% dilution of 29:1 acrylamide/bis-acrylamide was mixed with 0.1% ammonium persulfate (Sigma) and 0.01% TEMED (Sigma) as polymerization initiators. This mixture was then poured in a cavity placed on top of the master mold and allowed to polymerize for 2 h, while the cavity was sealed with a mechanically clamped silanized coverslip. Unpolymerized acrylamide was removed by washing microchamber arrays at least three times for at least 3 h each in distilled water, to prevent developmental arrest due to the toxicity of monomeric acrylamide, and subsequently stored in distilled water. Microchamber dimensions were 190 × 190 x 10 µm for heat stress and osmotic stress experiments, while 190 × 190 x 6 µm were used for starvation experiments. Prior to time-lapse imaging, microchamber arrays were incubated in M9 buffer for at least 4 hr for all conditions except osmotic shock. Instead, for osmotic shock microchamber arrays were stored in 200, 300 or 400 mM NaCl solutions for at least one week prior to the experiment. To load microchambers, a single microchamber array was placed with openings upwards on 76 × 26 × 1 mm microscope slide, within a glass spacer of the same height as the microchamber array. For all conditions except starvation, a drop of bacterial suspension containing a single late-stage embryo was transferred from a NGM agar plate seeded with OP50 bacteria into an individual microchamber, using an eyelash attached to a Pasteur pipette. Subsequently, more bacterial suspension was transferred until the microchamber was completely filled. For starvation, eggs were isolated by bleaching to remove bacteria and transferred to microchambers filled with M9 buffer. Finally, a 25 × 75 mm #1 coverslip was placed on top of the spacer and microchamber array. The resulting array of coverslips and spacers was sealed by high vacuum grease (Dow Corning) and mechanical clamping through a custom-fabricated holder, to prevent liquid evaporation during the duration of the experiment. A more detailed step-by-step procedure for embryo loading is found in ref. 38.

C. elegans time-lapse microscopy

We performed time-lapse imaging on a Nikon Ti-E inverted microscope. A large chip camera (Hamamatsu sCMOS Orca v2) ensured that single microchambers fitted in the field of view of the camera while using a 60 x magnification objective (Nikon CFI Plan Fluor 60 x, NA = 0.5-1.25, oil immersion). We used a custom-built microscopy set-up, described in ref. 38, that is optimized for rapid wide-field imaging, to prevent artifacts due to animal motion during exposure. Transmitted light images were captured using a red LED (CoolLED pE-100 615 nm) and fluorescence images using a 488 nm laser (Coherent OBIS LS 488-100) and a 561 nm laser (Coherent OBIS LS 561-100). For long-term time-lapse imaging, we used (80–100 mW) laser power and 1–10 ms exposure time, to typically capture a single imaging volume, consisting of ~9 Z-slices in three channels (transmitted light, 488 nm, 561 nm) every 15 minutes, for 10–20 animals imaged in parallel, using the Perfect Focus system to minimize sample drift. Hatching was defined as the first frame where the larvae appeared outside the egg shell, with manually annotated hatching time used as the start of time courses. NaCl can possibly already permeate the egg shell ~1 hour prior to hatching, due to softening of the egg shell[85], resulting in an onset of osmotic stress just before hatching. Indeed, at high salt concentrations, we observed that a fraction of embryos (3/18 at 300 and 10/32 at 400 mM NaCl) did not hatch normally but did display DAF-16/FOXO translocation dynamics, in which case the cessation of NaCl-induced embryonic motility was interpreted as hatching for analysis.

Temperature control

A temperature control system was used to maintain a constant temperature of 20 °C inside the sample. A thermoelectric chiller (Thermotek T257P) was used to cool the custom-made objective jacket by circulating an antifreeze fluid (a mixture of water and glycerin) between the chiller and the objective jacket. In order to calibrate the system, a thermocouple temperature sensor measuring 0.025 mm in diameter (RS Pro) was placed inside the sample in contact with the polyacrylamide hydrogel and connected to a digital thermometer (RS Pro). The temperature was then varied on the thermoelectric chiller while the resulting temperature inside the sample was being monitored. As animals in different microchambers hatch at slightly different times, the time after hatching at which the shift in temperature was initiated varied between animals. For the heat stress experiments, animals were allowed to hatch at 20 °C, followed by a sudden temperature increase to 31, 32 or 33 °C within 5 hours after hatching. For the heat interval experiments, custom-written software was used to automatically switch between 20 °C and the desired heat stress temperature.

Segmentation of intestinal cell nuclei and cytoplasm

Custom Python software was used to calculate DAF-16::GFP fluorescence intensity in the nucleus and cytoplasm of intestinal cells. We processed the H1-wCherry signal (marker for intestinal nuclei) in order to obtain precise boundaries of each cell's nucleus. First, the image z-stack for each time point was reduced to the maximum intensity projection, and the worm was segmented from the background using the Otsu method. To speed up computation time, the projected image was cropped to a rectangular region encompassing only the worm, thus removing most background areas. Next, the edges of individual nuclei were detected from the image gradient, which was calculated using the Sobel filter. Finally, a watershed segmentation algorithm was applied to the image gradient to isolate and label the nuclei and to generate a binary mask (see Fig. S1B). For each individual nucleus, the focal plane with the maximum average fluorescence intensity was automatically detected and selected as the optimal focal plane. To obtain the cytoplasmic region, the nuclear mask was first expanded by dilation (7 pixels) and subsequently subtracted from the expanded mask, resulting in a narrow ring surrounding the nucleus. Finally, for each cell the average fluorescence intensity inside the nuclear mask, I_{nucl}, and inside the cytoplasmic mask, I_{cyt}, was evaluated at the optimal focal plane. To analyze DAF-16::GFP in individual intestinal cell independently, segmented cells were manually annotated, by first outlining the nuclear mask and subsequently outlining a small area in the cytoplasm directly adjacent to the nuclear mask. For the analysis of *akt-1* mutants, only the Int2D and int2V cells were analyzed. All time-lapse movies were carefully inspected by eye and showed no disagreement with DAF-16 localization trajectories obtained by automatic quantification.

Quantification of DAF-16 localization

DAF-16::GFP subcellular localization in intestinal cells was quantified as the ratio $R = \frac{I_{nucl}}{I_{cyt}}$. Since DAF-16 localization trajectories appeared almost identical in all intestinal cells at a 15-minute time resolution, they were averaged for the ease of analysis, unless otherwise stated. To perform quantitative analysis of pulsatile dynamics, we first needed to discriminate nuclear from cytoplasmic localization of DAF-16. For animals under starvation and osmotic stress, we defined a threshold by calculating the average R of animals in the control condition (20 °C *ad libitum* food in the absence of stress) and multiplying by a factor of 1.05. Due to the persistent nuclear localization of DAF-16 in animals under heat stress, we used a higher threshold of $R = 1.1$.

Quantification of DAF-16/FOXO target gene expression

To quantify DAF-16/FOXO target gene expression, we first generated a maximum intensity projection from the image z-stack of the fluorescent reporter channel for each time point in the time-lapse movie. From this projection, we selected the top 2.5% of pixels with the highest fluorescence intensity and calculated their mean intensity.

Analysis of pulse characteristics

DAF-16 pulses under osmotic stress were characterized by their duration and amplitude. For each pulse, duration was defined as the time the $R(t)$ value was uninterruptedly above the threshold ($R > R_{control}*1.05$). Pulse amplitude was defined as the maximum $R(t)$ value within each pulse. To differentiate true pulses from inherent variability and measurement noise, we only took pulses into account that lasted longer than a single time-point. Amplitude was defined as the maximum R value during each uninterrupted pulse. The amplitude of the initial nuclear peak upon heat stress was characterized by finding the maximum $R(t)$ value within 3 hours after the onset of heat stress. The fraction of time DAF-16 is nuclear ϕ was calculated as the number of time points DAF-16 is nuclear versus the total number of time points after onset of heat stress.

Measurements of *C. elegans* body length and growth analysis

We used body length over time as a proxy for growth. In order to measure the body length of worms, ~10 points were manually placed along the worms' proximal-distal axis, and a spline was fit through the points at each time point. The growth rate was defined as $\frac{\Delta L}{\Delta T}$, where ΔL is the change of body length measured over the interval ΔT. Here, ΔT was the time between hatching and the end of the time-lapse movie, and varied in value between individuals depending, e.g., on whether the animal's full body was in view for body length analysis. The reported fraction of time ϕ that DAF-16::GFP was nuclear was then determined over the same time interval. A Savitzky-Golay filter was used to smooth data for presentation, using a window length of 19 and a polynomial order of 3.

Monte Carlo simulation for determining lag time uncertainties

To detect potential cell-to-cell delays in DAF-16::GFP translocation dynamics, we computed cell-pair cross-correlations and quantified the lag time as the position of the cross-correlation maximum. The peak position is subject to uncertainties due to the propagation of measurement error, intrinsic cellular noise, and a finite sampling rate. Large uncertainties in the peak position challenge the fact that any observed lag is 'real', i.e., whether a non-zero lag is statistically significant. Uncertainties in the cross-correlation lag times were estimated using the following model-independent Monte Carlo simulation[86]. A random set of N points was selected from the original time series data (also consisting of N points/measurements), regardless of whether any point was previously chosen. Points that were selected multiple times were only included once, thus reducing the size of the original set by ~35%. The temporal order of the sampled points was retained by re-ordering them after the random selection. The set was generated for the time series of two different cells, i.e., the same time points were selected for both signals, which were then cross-correlated and lag time obtained as the cross-correlation maximum. This procedure was iterated 2000 times, leading to a distribution of lag times. The mean of the distribution was used as the delay between any given pair of cells, and the 95% confidence interval as its error. If the confidence interval for any given cell-pair lag time included the value zero, the DAF-16 dynamics delay between the cells was considered not significant. As an additional control, N data points were randomly extracted from the time series, but not temporally re-ordered, and signals were cross-correlated. The peak position histogram after 1000 iterations displayed a sharp peak at zero, which confirmed that the observed delays are not an artifact.

Construction of GFP-FOXO3A plasmid

A human *FOXO3A* cDNA fragment (GenBank: AY892951) was obtained from pDNR-DUAL-HsCD00005232 (cDNA clone HsCD00005232 of the human FOXO3 gene inserted into plasmid pDNR-Dual) by digestion with the restriction enzymes *Sal*I and *Xba*I. This fragment was cloned into pEGFP-C1 (Clontech Laboratories) to generate the GFP-FOXO3A plasmid. This plasmid is available upon request from María Olmedo.

Cell culture

U2OS H2B-RFP7 Hygroo-1 cells were a gift from Dr. Israel Salguero, a member of Dr. Steve Jackson's laboratory. U2OS cells were originally obtained from the ATCC cell repository and were authenticated at the lab of origin by STR profiling. Cells were grown in Dulbecco's modified Eagle medium (DMEM) supplemented with 10% fetal calf serum (FBS) and 2 mM L-glutamine (Sigma-Aldrich). Cells were maintained in a 5% CO_2 humidified atmosphere at 37 °C. U2OS cells were transiently transfected with GFP-FOXO3A expression plasmid.

Transient transfection of human epithelial cells

U2OS cells were transfected by electroporation using the GFP-FOXO3A expression plasmid. Briefly, approximately 10^7 cells were trypsinized, washed with cold PBS, and then resuspended in 200 µl of DMEM supplemented with 15 mM HEPES pH 7.4. 6 µg of plasmid DNA was mixed with H_2O and NaCl (final concentration of 200 mM) in 50 µl of final volume, and added to the cell suspension. The cell–DNA mixture was then incubated on ice for 10 min and electroporated using a Gene Pulser Xcell (BioRad) at a setting of 950 µF, 720 Ω, and 240 V in 0.4-cm transfection cuvettes. Cells were incubated on ice for an additional 10 min, diluted 1:20 in DMEM supplemented with 10% FBS, and seeded into µ-slide 8-well plates (Ibidi). Transfected human cells were incubated at 37 °C with 5% CO_2.

FBS starvation assay

24 hours after electroporation transfections, cells were washed twice PBS and incubated in a fresh medium without phenol red and supplemented with 2 mM glutamine (Sigma-Aldrich). Different amounts of FBS were added to the fresh medium when the effect of FBS was analyzed. After 15 minutes, 8-well plates containing epithelial cells expressing GFP-FOXO3A were placed in a fluorescence microscope equipped with an incubation system, and images were captured.

Cell culture fluorescence microscopy

Images were captured with a Zeiss Apotome fluorescence microscope equipped with a 10x Plan Apochromat objective and an incubation system that covers every requirement in the cultivation and observation of living cells (37 °C; 5% CO_2). Pictures were taken at 20 or 40 min intervals using an Axiocam 506 camera, and the images were analyzed using ImageJ software (Wayne Rasband, Research Services Branch, National Institute of Mental Health, MD, USA).

Quantification of GFP-FOXO3A dynamics

GFP-FOXO3A nuclear localization was quantified using ImageJ (FIJI). We measured the mean fluorescence signal in regions of the same size, in the nucleus and cytoplasm. We calculated R as the ratio of the signal of the nucleus to that of the cytoplasm. The graphs show the values for 13-19 cells per condition, obtained in three independent experiments.

Statistics and reproducibility

No statistical method was used to predetermine sample size. Instead, sample size and experiment duration were chosen to sufficiently sample the observed stochastic translocation dynamics. For *C. elegans* experiments, some data were excluded based on the following criteria. In general, animals were excluded that were out-of-focus and outside of the microchamber for the majority of the duration of the time-lapse experiments. For growth analysis, animals were excluded when part of the body was outside the field of view for the majority of the duration of the experiment, or on key predetermined analysis time points (e.g., 0, 5, 10 and 15 hours after hatching). We excluded all animals where due to loading mistakes, more than one egg was loaded, even if one of those eggs was not viable, as we found that the presence of unviable eggs changed DAF-16/FOXO translocation dynamics in particular under starvation, likely by release of nutrient signals. For cell culture experiments, cells that exited the field of view rapidly or died during the experiment. The experiments were randomized, as *C. elegans* embryos or U2OS cells were randomly assigned to the different stress conditions. The investigators were not blinded to allocation during experiments and outcome assessment. The representative microscopy images in Figs. 1C–E, 4B and SI Figs. 1D, H, 3A, C, 6A, were independently repeated between 5–20 times, with qualitatively similar results.

Reporting summary

Further information on research design is available in the Nature Portfolio Reporting Summary linked to this article.

Data availability

The raw imaging data reported in this study cannot be deposited in a public repository due to its size. To request access, contact the corresponding author. All analyzed data and analysis code needed to recreate all figures are deposited at Zenodo[87] under accession code https://doi.org/10.5281/zenodo.17399524. Analyzed data for all animals in Figs. 1–6 and Figures S1,S2 are included in the Source Data file. Source data are provided with this paper.

Code availability

All analyzed data and analysis code needed to recreate all figures are deposited at Zenodo[87] under accession code https://doi.org/10.5281/zenodo.17399524.

References

1. Puig, O. et al. Control of cell number by Drosophila FOXO: downstream and feedback regulation of the insulin receptor pathway. Genes Dev. **17**, 2006–2020 (2003).
2. Baker, J. et al. Role of insulin-like growth factors in embryonic and postnatal growth. Cell **75**, 73–82 (1993).
3. Brogiolo, W. et al. An evolutionarily conserved function of the Drosophila insulin receptor and insulin-like peptides in growth control. Curr. Biol. **11**, 213–221 (2001).
4. Liu, J. P. et al. Mice carrying null mutations of the genes encoding insulin-like growth factor I (Igf-1) and type 1 IGF receptor (Igf1r). Cell **75**, 59–72 (1993).
5. Shingleton, A. W. et al. The temporal requirements for insulin signaling during development in Drosophila. PLoS Biol. **3**, e289 (2005).
6. Tennessen, J. M. & Thummel, C. S. Coordinating growth and maturation - insights from Drosophila. Curr. Biol. **21**, R750–R757 (2011).
7. Baugh, L. R. To grow or not to grow: nutritional control of development during Caenorhabditis elegans L1 arrest. Genetics **194**, 539–555 (2013).
8. Gui, T. & Burgering, B. M. T. FOXOs: masters of the equilibrium. FEBS J. **289**, 7918–7939 (2022).
9. Brunet, A. et al. Akt promotes cell survival by phosphorylating and inhibiting a Forkhead transcription factor. Cell **96**, 857–868 (1999).
10. Kops, G. J. et al. Forkhead transcription factor FOXO3a protects quiescent cells from oxidative stress. Nature **419**, 316–321 (2002).
11. Nemoto, S., Fergusson, M. M. & Finkel, T. Nutrient availability regulates SIRT1 through a forkhead-dependent pathway. Science **306**, 2105–2108 (2004).
12. Tran, H. et al. DNA repair pathway stimulated by the forkhead transcription factor FOXO3a through the Gadd45 protein. Science **296**, 530–534 (2002).
13. Tokarz, V. L., MacDonald, P. E. & Klip, A. The cell biology of systemic insulin function. J. Cell Biol. **217**, 2273–2289 (2018).
14. Andersen, D. S., Colombani, J. & Léopold, P. Coordination of organ growth: principles and outstanding questions from the world of insects. Trends Cell Biol. **23**, 336–344 (2013).
15. Petersen, M. C. & Shulman, G. I. Mechanisms of Insulin Action and Insulin Resistance. Physiol. Rev. **98**, 2133–2223 (2018).
16. Willcox, B. J. et al. FOXO3A genotype is strongly associated with human longevity. Proc. Natl. Acad. Sci. USA **105**, 13987–13992 (2008).
17. Poloz, Y. & Stambolic, V. Obesity and cancer, a case for insulin signaling. Cell Death Dis. **6**, e2037 (2015).
18. Suh, Y. et al. Functionally significant insulin-like growth factor I receptor mutations in centenarians. Proc. Natl. Acad. Sci. USA **105**, 3438–3442 (2008).
19. Gross, D. N., Wan, M. & Birnbaum, M. J. The role of FOXO in the regulation of metabolism. Curr. Diab Rep. **9**, 208–214 (2009).
20. Baugh, L. R. & Sternberg, P. W. DAF-16/FOXO regulates transcription of cki-1/Cip/Kip and repression of lin-4 during C. elegans L1 arrest. Curr. Biol. **16**, 780–785 (2006).
21. Burton, N. O. et al. Insulin-like signalling to the maternal germline controls progeny response to osmotic stress. Nat. Cell Biol. **19**, 252–257 (2017).
22. Murphy, C. T. and P.J. Hu, Insulin/insulin-like growth factor signaling in C. elegans. WormBook, p. 1–43 (2013).
23. Ogg, S. et al. The Fork head transcription factor DAF-16 transduces insulin-like metabolic and longevity signals in C. elegans. Nature **389**, 994–999 (1997).
24. Weinkove, D. et al. Long-term starvation and ageing induce AGE-1/PI 3-kinase-dependent translocation of DAF-16/FOXO to the cytoplasm. BMC Biol. **4**, 1 (2006).
25. Paradis, S. & Ruvkun, G. Caenorhabditis elegans Akt/PKB transduces insulin receptor-like signals from AGE-1 PI3 kinase to the DAF-16 transcription factor. Genes Dev. **12**, 2488–2498 (1998).
26. Rena, G. et al. Phosphorylation of the transcription factor forkhead family member FKHR by protein kinase B. J. Biol. Chem. **274**, 17179–17183 (1999).
27. Lee, R. Y., Hench, J. & Ruvkun, G. Regulation of C. elegans DAF-16 and its human ortholog FKHRL1 by the daf-2 insulin-like signaling pathway. Curr. Biol. **11**, 1950–1957 (2001).
28. Furuyama, T. et al. Identification of the differential distribution patterns of mRNAs and consensus binding sequences for mouse DAF-16 homologues. Biochem J. **349**, 629–634 (2000).
29. Schuster, E. et al. DamID in C. elegans reveals longevity-associated targets of DAF-16/FoxO. Mol. Syst. Biol. **6**, 399 (2010).
30. Tepper, R. G. et al. PQM-1 complements DAF-16 as a key transcriptional regulator of DAF-2-mediated development and longevity. Cell **154**, 676–690 (2013).
31. Kaplan, R. E. W. et al. Food perception without ingestion leads to metabolic changes and irreversible developmental arrest in C. elegans. BMC Biol. **16**, 112 (2018).
32. Mata-Cabana, A. et al. Social chemical communication determines recovery From L1 Arrest via DAF-16 Activation. Front Cell Dev. Biol. **8**, 588686 (2020).
33. Henderson, S. T. & Johnson, T. E. daf-16 integrates developmental and environmental inputs to mediate aging in the nematode Caenorhabditis elegans. Curr. Biol. **11**, 1975–1980 (2001).
34. Alam, H. et al. EAK-7 controls development and life span by regulating nuclear DAF-16/FoxO activity. Cell Metab. **12**, 30–41 (2010).
35. Putker, M. et al. Redox-dependent control of FOXO/DAF-16 by transportin-1. Mol. Cell **49**, 730–742 (2013).
36. Riedel, C. G. et al. DAF-16 employs the chromatin remodeller SWI/SNF to promote stress resistance and longevity. Nat. Cell Biol. **15**, 491–501 (2013).
37. Wolff, S. et al. SMK-1, an essential regulator of DAF-16-mediated longevity. Cell **124**, 1039–1053 (2006).
38. Gritti, N. et al. Long-term time-lapse microscopy of C. elegans post-embryonic development. Nat. Commun. **7**, 12500 (2016).
39. Aghayeva, U., A. Bhattacharya, and O. Hobert, A panel of fluorophore-tagged daf-16 alleles. *MicroPubl. Biol*. **2020**, (2020).
40. Lasick, K. A. et al. FOXO nuclear shuttling dynamics are stimulus-dependent and correspond with cell fate. Mol. Biol. Cell **34**, ar21 (2023).
41. Jia, C., Qian, H. & Zhang, M. Q. Exact power spectrum in a minimal hybrid model of stochastic gene expression oscillations. SIAM J. Appl. Math. **84**, 1204–1226 (2024).
42. Kimura, K. D. et al. daf-2, an insulin receptor-like gene that regulates longevity and diapause in Caenorhabditis elegans. Science **277**, 942–946 (1997).
43. Kwon, E. S. et al. A new DAF-16 isoform regulates longevity. Nature **466**, 498–502 (2010).
44. Tomioka, M. et al. The insulin/PI 3-kinase pathway regulates salt chemotaxis learning in Caenorhabditis elegans. Neuron **51**, 613–625 (2006).
45. Lev, I. et al. Germ granules govern small RNA inheritance. Curr. Biol. **29**, 2880–2891.e4 (2019).

46. Padmanabhan, S. et al. A PP2A regulatory subunit regulates C. elegans insulin/IGF-1 signaling by modulating AKT-1 phosphorylation. Cell **136**, 939–951 (2009).
47. Greer, E. L. et al. An AMPK-FOXO pathway mediates longevity induced by a novel method of dietary restriction in C. elegans. Curr. Biol. **17**, 1646–1656 (2007).
48. Lee, H. et al. The Caenorhabditis elegans AMP-activated protein kinase AAK-2 is phosphorylated by LKB1 and is required for resistance to oxidative stress and for normal motility and foraging behavior. J. Biol. Chem. **283**, 14988–14993 (2008).
49. Schindler, A. J., Baugh, L. R. & Sherwood, D. R. Identification of late larval stage developmental checkpoints in Caenorhabditis elegans regulated by insulin/IGF and steroid hormone signaling pathways. PLoS Genet. **10**, e1004426 (2014).
50. Fukuyama, M. et al. The C. elegans Hypodermis Couples Progenitor Cell Quiescence to the Dietary State. Curr. Biol. **25**, 1241–1248 (2015).
51. Uppaluri, S., Weber, S. C. & Brangwynne, C. P. Hierarchical size scaling during multicellular growth and development. Cell Rep. **17**, 345–352 (2016).
52. Muñoz, M. J. & Riddle, D. L. Positive selection of Caenorhabditis elegans mutants with increased stress resistance and longevity. Genetics **163**, 171–180 (2003).
53. Stojanovski, K., Großhans, H. & Towbin, B. D. Coupling of growth rate and developmental tempo reduces body size heterogeneity in C. elegans. Nat. Commun. **13**, 3132 (2022).
54. Uppaluri, S. & Brangwynne, C. P. A size threshold governs Caenorhabditis elegans developmental progression. Proc. Biol. Sci. **282**, 20151283 (2015).
55. Lamitina, S. T. et al. Adaptation of the nematode Caenorhabditis elegans to extreme osmotic stress. Am. J. Physiol. Cell Physiol. **286**, C785–C791 (2004).
56. Lindner, B. et al. Effects of noise in excitable systems. Phys. Rep. **392**, 321–424 (2004).
57. Hibshman, J. D., et al. daf-16/FoxO promotes gluconeogenesis and trehalose synthesis during starvation to support survival. *Elife*, **6**, (2017).
58. Oh, S. W. et al. Identification of direct DAF-16 targets controlling longevity, metabolism and diapause by chromatin immunoprecipitation. Nat. Genet **38**, 251–257 (2006).
59. Essers, M. A. et al. Functional interaction between beta-catenin and FOXO in oxidative stress signaling. Science **308**, 1181–1184 (2005).
60. Hsu, A. L., Murphy, C. T. & Kenyon, C. Regulation of aging and age-related disease by DAF-16 and heat-shock factor. Science **300**, 1142–1145 (2003).
61. Link, C. D. et al. Direct observation of stress response in Caenorhabditis elegans using a reporter transgene. Cell Stress Chaperones **4**, 235–242 (1999).
62. Frøkjær-Jensen, C. et al. Improved Mos1-mediated transgenesis in C. elegans. Nat. Methods **9**, 117–118 (2012).
63. Calnan, D. R. & Brunet, A. The FoxO code. Oncogene **27**, 2276–2288 (2008).
64. Huang, H. & Tindall, D. J. Dynamic FoxO transcription factors. J. Cell Sci. **120**, 2479–2487 (2007).
65. De Simone, A. et al. Control of osteoblast regeneration by a train of Erk activity waves. Nature **590**, 129–133 (2021).
66. de la Cova, C. et al. A real-time biosensor for ERK activity reveals signaling dynamics during C. elegans Cell Fate Specification. Dev. Cell **42**, 542–553.e4 (2017).
67. Böhni, R. et al. Autonomous control of cell and organ size by CHICO, a Drosophila homolog of vertebrate IRS1-4. Cell **97**, 865–875 (1999).
68. Kramer, J. M. et al. Expression of Drosophila FOXO regulates growth and can phenocopy starvation. BMC Dev. Biol. **3**, 5 (2003).
69. Miron, M. et al. The translational inhibitor 4E-BP is an effector of PI(3)K/Akt signalling and cell growth in Drosophila. Nat. Cell Biol. **3**, 596–601 (2001).
70. Radimerski, T. et al. dS6K-regulated cell growth is dPKB/dPI(3)K-independent, but requires dPDK1. Nat. Cell Biol. **4**, 251–255 (2002).
71. Kang, C. & Avery, L. Systemic regulation of starvation response in Caenorhabditis elegans. Genes Dev. **23**, 12–17 (2009).
72. Kageyama, R. et al. Oscillatory gene expression and somitogenesis. Wiley Interdiscip. Rev. Dev. Biol. **1**, 629–641 (2012).
73. Fernandes de Abreu, D. A. et al. An insulin-to-insulin regulatory network orchestrates phenotypic specificity in development and physiology. PLoS Genet **10**, e1004225 (2014).
74. Kaplan, R. E. W. et al. Pervasive Positive and Negative Feedback Regulation of Insulin-Like Signaling in Caenorhabditis elegans. Genetics **211**, 349–361 (2019).
75. Murphy, C. T., Lee, S. J. & Kenyon, C. Tissue entrainment by feedback regulation of insulin gene expression in the endoderm of Caenorhabditis elegans. Proc. Natl. Acad. Sci. USA **104**, 19046–19050 (2007).
76. Tissenbaum, H. A. DAF-16: FOXO in the Context of C. elegans. Curr. Top. Dev. Biol. **127**, 1–21 (2018).
77. Zhou, K. I., Pincus, Z. & Slack, F. J. Longevity and stress in Caenorhabditis elegans. Aging **3**, 733–753 (2011).
78. Li, J. et al. Caenorhabditis elegans HCF-1 functions in longevity maintenance as a DAF-16 regulator. PLoS Biol. **6**, e233 (2008).
79. Levine, J. H., Lin, Y. & Elowitz, M. B. Functional roles of pulsing in genetic circuits. Science **342**, 1193–1200 (2013).
80. Purvis, J. E. & Lahav, G. Encoding and decoding cellular information through signaling dynamics. Cell **152**, 945–956 (2013).
81. Venkatachalam, V., Jambhekar, A. & Lahav, G. Reading oscillatory instructions: How cells achieve time-dependent responses to oscillating transcription factors. Curr. Opin. Cell Biol. **77**, 102099 (2022).
82. Hansen, A. S. & O'Shea, E. K. Promoter decoding of transcription factor dynamics involves a trade-off between noise and control of gene expression. Mol. Syst. Biol. **9**, 704 (2013).
83. Litvak, V. et al. Function of C/EBPdelta in a regulatory circuit that discriminates between transient and persistent TLR4-induced signals. Nat. Immunol. **10**, 437–443 (2009).
84. Murphy, L. O. et al. Molecular interpretation of ERK signal duration by immediate early gene products. Nat. Cell Biol. **4**, 556–564 (2002).
85. Singh, R. & Sulston, J. Some observations on moulting in Caenorhabditis elegans. Nematologica **24**, 63–71 (1978).
86. Peterson, B. M. et al. On Uncertainties in cross-correlation lags and the reality of wavelength-dependent continuum lags in active galactic nuclei. Publ. Astron. Soc. Pac. **110**, 660 (1998).
87. van Zon, J., Demirbas, B., & Filina, O., *Data set for the article "Body-wide synchronization of insulin-signaling dependent DAF-16/FOXO nuclear translocation pulses correlated with C. elegans growth"*. Zenodo. https://doi.org/10.5281/zenodo.17399524 (2025).

Acknowledgements

We thank Peter Askjaer, Tom Shimizu, Pieter Rein ten Wolde, and Sander Tans for comments and critical reading of the manuscript. Initial observations of pulses were performed at the lab of J.v.Z during a COST GENiE Short Term Scientific Mission COST-STSM-BM1408-35915 (M.O.). Research was further funded by the Dutch Research Council (NWO) through the VIDI grant 680-47-529 (O.F., Y.G., J.v.Z.) and the project OCENW.KLEIN.072 (T.L.), the grant PID2022-139009OB-I00 (M.O.) funded by MICIU/AEI/10.13039/501100011033 and by "ERDF a way of making Europe" and the VI Research Plan of the University of Sevilla (PPIT-US, M.A.S-R.). Some strains were provided by the Caenorhabditis Genetics Center (CGC), which is supported by the National Institutes of Health-Office of Research Infrastructure Programs (P40 OD010440).

Author contributions

O.F., B.D., M.O., and J.v.Z. conceived the research. O.F., B.D., M.O., and J.v.Z. wrote the manuscript with the input and discussion of all authors. O.F., B.D., T.L., A.N., Y.G., and M.O. performed *C. elegans* experiments. M.A.S-R. performed cell culture experiments. O.F., B.D., and T.L. performed analysis of microscopy data. O.F. and B.D. developed Python scripts to perform most data analysis.

Competing interests

The authors declare no competing interests.

Additional information

Supplementary information The online version contains supplementary material available at https://doi.org/10.1038/s41467-025-66164-2.

Correspondence and requests for materials should be addressed to María Olmedo or Jeroen S. van Zon.

Peer review information *Nature Communications* thanks the anonymous reviewer(s) for their contribution to the peer review of this work. A peer review file is available.

Reprints and permissions information is available at http://www.nature.com/reprints